Tectonophysics 890 (2024) 230472

Contents lists available at ScienceDirect

Tectonophysics

journal homepage: www.elsevier.com/locate/tecto

The influence of the strength of pre-existing weak zones on rift geometry and strain localization

Liang Xue [a,*], Robert Moucha [a], Folarin Kolawole [b], James D. Muirhead [c], Christopher A. Scholz [a]

[a] Department of Earth and Environmental Sciences, Syracuse University, United States
[b] Department of Earth and Environmental Sciences, Columbia University, United States
[c] School of Environment, University of Auckland, New Zealand

ARTICLE INFO

Keywords:
Oblique rift
Continental rift
Geodynamic model
Weak zone
Segmentation

ABSTRACT

Continental rifts normally initiate within previously deformed lithosphere and thus their evolution and architecture can be largely controlled by inherited weak zones in the pre-rift crust. Here, we quantify the role of the strength and obliquity of pre-existing crustal-scale weak zones in the evolution of continental rift systems. We use a 3D numerical geodynamic model to assess strain localization, associated fault development, and rift segmentation during the early stages of tectonic extension. We find that both the strength and obliquity of the weak zones significantly influence the patterns of strain localization. A pre-existing very weak zone with low obliquity can promote the development of continuous and long-lived border faults parallel to the rift axis. Conversely, a comparatively strong weak zone with high obliquity leads to a staggered en-echelon rift geometry that lacks rectilinear laterally persistent strain localization. Furthermore, we find that rift obliquity and weak zone strength may modulate rift fault length, throw, and azimuth. These results provide new and compelling insights into the structure and evolution of natural active rifts that develop within orogenic basement terranes.

1. Introduction

Continental rifting is a fundamental plate tectonic process and a key stage of the Wilson Cycle. Inception and evolution of continental rifts is known to be strongly influenced by inherited heterogeneities of different scales that include lithospheric-scale suture zones, foliations, shear zones, and local-scale structures such as folds, faults, and dykes (e.g., Corti et al., 2022; Kolawole et al., 2018; Laó-Dávila et al., 2015; Van Wijk, 2005; Molnar et al., 2019; Zwaan and Schreurs, 2017, 2020). Here, we employ the term "pre-existing weak zones" that encompasses all these inherited structures to describe regions of reduced mechanical strength, resulting from past orogenic or intraplate processes at the lithosphere scale (e.g., Corti, 2008; Gueydan et al., 2008; Molnar et al., 2019). Natural rift systems that exhibit a wide range of relationships between these lithospheric-scale pre-existing weak zones and rift architecture include, for example, the Rhine Graben (Michon and Merle, 2000), the Rio Grande Rift (Morgan et al., 1986), the Main Ethiopian Rift (Corti et al., 2018), the Malawi Rift (Kolawole et al., 2018; Laó-Dávila et al., 2015; Grijalva et al., 2018), and the Red Sea (Molnar et al., 2019).

The orientation of the pre-existing weak zones can largely influence strain localization during rift evolution and result in oblique rifting, when the divergence direction is not perpendicular to the weak zone (e.g., Brune, 2014). These oblique rifts are characterized by an angle between the divergence direction and the direction perpendicular to the axis (here and after referred to as rift obliquity, Fig. 1f). Most present-day rifts and ridges exhibit some degree of obliquity (Fig. 1), such as the Lake Tanganyika Rift (Fig. 1a; Molnar et al., 2019; Versfelt and Rosendahl, 1989), Main Ethiopian Rift (Fig. 1b Corti et al., 2013), Gulf of Aden (Fig. 1c; Bellahsen et al., 2013; Jourdon et al., 2020), Gulf of California (Fig. 1d; Bonini et al., 2019), Malawi Rift (Chorowicz and Sorlien, 1992), South China Sea (Le Pourhiet et al., 2017), and Aegean Rift (Agostini et al., 2010). It is also suggested that orthogonal rifts are possibly just a temporary stage in the evolution of continental rifts (e.g., Brune et al., 2018).

Rift obliquity appears to impact the timing, patterns, and nature of rift faulting (e.g., Ebinger and van Wijk, 2014; Philippon and Corti, 2016; Withjack et al., 2002). Oblique rifting commonly leads to variable rift axis orientations along strike, segmented border faults, and/or rotation of intrarift faults (e.g., Díaz-Azpiroz et al., 2016; McClay and White, 1995). For example, in the Main Ethiopian Rift (Fig. 1b) the northern segment exhibits an obliquity of ~45° and is characterized by oblique boundary faults with a strike-slip component, whereas the

* Corresponding author.
E-mail address: lxue07@syr.edu (L. Xue).

https://doi.org/10.1016/j.tecto.2024.230472
Received 20 November 2023; Received in revised form 5 August 2024; Accepted 18 August 2024
Available online 20 August 2024

southern segment of the Main Ethiopian Rift, with an obliquity ~10°, is dominated by dip-slip intrarift faults (e.g., Agostini et al., 2011; Corti et al., 2013). Herein, we define a rift segment as a distinct laterally continuous rectilinear (or sub-rectilinear) rift basin, such that rift systems with staggered shorter-length rift basins are described as 'highly segmented', and those with laterally persistent rectilinear segments that form relatively longer basins are described to have lateral persistent strain localization. Different from the low-moderate obliquity rift segments in Ethiopia, the Gulf of California is characterized by a highly oblique (~70°) divergent boundary between the Pacific and North American plates that has progressed to sea floor spreading (Fig. 1d), with strain accommodated by a group of en-echelon strike-slip faults within the oceanic pull apart basins (Ferrari, 2013).

Kinematic, analogue (physical), and numerical models are often adopted to conduct rifting experiments and to explore the influence of pre-existing weak zones on rift evolution. Kinematic models and their interpretations of oblique rift geometry, faults, and block movements (Courtillot, 1982; Heine and Brune, 2014; Le Pourhiet et al., 2017; Vink, 1982) are constructed using geological observations of rift structure (Argus et al., 2011) and inferred geodetic and paleomagnetic observations (Kreemer et al., 2003). Such models are often applied to reconstruct the plate motion of rift systems and can be used for statistical analysis of strain partitioning along plate boundaries (Brune et al., 2018; Heine and Brune, 2014; Müller et al., 2016; Philippon and Corti, 2016).

Analogue models can also provide valuable insights into the geometry and formation of rifts and ridges within pre-existing weak zones (e.g., Agostini et al., 2009, 2011; Basile and Brun, 1999; Bonini et al., 1997, 2023; Clifton et al., 2000; Corti et al., 2003, Corti, 2008; Corti et al., 2011; Dauteuil and Brun, 1993; Henza et al., 2011; Molnar et al., 2018, 2019, 2020; Osagiede et al., 2021; Richetti et al., 2023; Samsu et al., 2023; Withjack et al., 2002; Zou et al., 2024; Zwaan and Schreurs, 2017, 2020; Zwaan et al., 2018, 2020; Zwaan et al., 2021; Zwaan et al., 2022). For example, Dauteuil et al. (2002) used analogue models to explore the role of lithospheric strength, weak zone, and divergence direction in the evolution of oblique rifts and concluded that major transform faults associated with fast-spreading ridges are formed by diffuse, complex arrays of strike-slip segments, while transform faults associated with slow-spreading ridges form deep, narrow linear valleys. Likewise, Autin et al. (2013) used a four-layer analogue model to investigate the evolution of the Gulf of Aden and proposed that the obliquity of rifted margin basins largely control the present-day rifted margin geometry and determine the location of oceanic transform faults. Whereas, Philippon et al. (2015) used an analogue model to investigate the relationship between dip-slip and strike-slip displacements along orthogonal and oblique faults corresponding to extension direction, and observed slip reorientation during oblique extension. More recently, analogue models tested the interaction between extensional direction, inherited structural orientation, and rift axis directions (e.g., Zou et al., 2024). Lastly, Zwaan et al. (2022) reviewed and evaluated the effects of both structural inheritance and kinematics (i.e. extension rate and direction) on oblique rift evolution, suggesting that the preferential patterns of reactivation of pre-existing weak zones is related to rift obliquity, lithospheric layering, and extension rates.

Numerical modeling can expand on these findings of analogue experiments by incorporating rheological complexities and surface processes that include erosion and sedimentation. Recently, a variety of 3D or 2.5D (2D surface models coupled with 2D geodynamic models) numerical models have been developed to investigate continental rifting (e.g., Allken et al., 2011 Andrés-Martínez et al., 2019; Brune et al., 2017a, 2017b; Brune et al., 2018; Corti et al., 2019; Dyksterhuis et al., 2007; Gouiza and Naliboff, 2021; Jourdon et al., 2020; Koptev et al., 2015; Liu et al., 2022; Maestrelli et al., 2022; Naliboff et al., 2020;

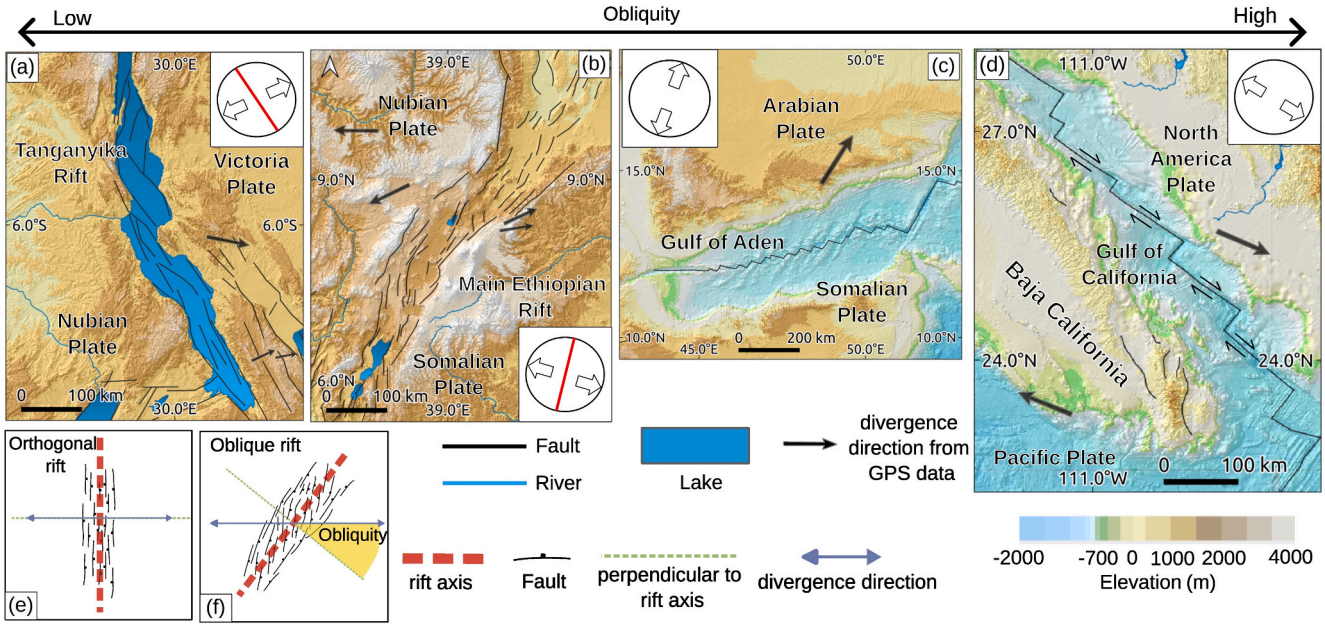

Fig. 1. (a-d) Natural examples of oblique rifts classified by the approximate obliquity from low (left) to high (right). Digital elevation model of topography and bathymetry are from Global Bathymetry and Topography at 15 Arc Sec (Tozer et al., 2019).The arrow shows the general divergence direction for Tanganyika Rift (Stamps et al., 2008; Stamps et al., 2018), Main Ethiopian Rift (Stamps et al., 2008; Corti et al., 2013), Gulf of Aden (Bellahsen et al., 2013), and Gulf of California (Plattner et al., 2007; Bonini et al., 2019). The faults are derived from Active Faults of Eurasia Database. The inset shows the divergence direction from principal stress component σ_3 from Delvaux and Barth (2010) and Cruz-Hernández et al. (2023). The red lines represent dike orientation from Wadge et al. (2016). (e, f) Illustration of rift obliquity, the angle between divergence direction and perpendicular to rift axis. The rift fault geometry for orthogonal rifts and oblique rifts (f) is derived and modified from analogue model results (Philippon and Corti, 2016). Notably, all the extension rates and directions shown here are derived present-day geodetic studies, which may not entirely reflect the initial rifting direction.

Neuharth et al., 2021, Neuharth et al., 2022; Njinju et al., 2021; Olive et al., 2022; Pichel et al., 2022; Rajaonarison et al., 2021; Schmid et al., 2023; Van Wijk, 2005). However, only a few numerical models have focused on investigating the role of pre-existing weak zones (e.g., Ammann et al., 2018; Duclaux et al., 2020; Glerum et al., 2020; Neuharth et al., 2021; Wolf et al., 2022). Brune et al. (2012) suggested that oblique extension can facilitate and possibly accelerate rifting processes, because oblique deformation requires less force to reach plastic yield strength than orthogonal extension. Brune (2014) later demonstrated that oblique extension can also generate multiple fault populations, with the number of orientations of fault systems varying depending on the angle of rift obliquity. Similarly, Duclaux et al. (2020) examined the effects of obliquity on normal fault development and identified phases of strain localization during rift evolution, where en-échelon faults form early and as rifting progresses, the faults link and develop into well-defined mid-ocean ridges. A study by Zwaan et al. (2016) combined analogue and 3D numerical models to demonstrate that orthogonal extension produced wider rifts compared to oblique rifting, which resulted in rift narrowing as obliquity increased. More recently, Naliboff et al. (2020) started with a randomly distributed weak zone and found that an initially distributed fault network tends to coalesce during extension, and that rift geometry in the later phases of extension was largely dependent on thermal and rheological properties rather than pre-existing structures. Further, numerical modeling of oblique rift segmentation revealed that individual rift segments can propagate towards each other under oblique extension, interacting (Allken et al., 2011; Van Wijk et al., 2017; Wolf et al., 2022) and/or forming a microplate between them, resembling the Victoria Plate in the East African Rift (Glerum et al., 2020; Neuharth et al., 2021). Such results also align with the outcomes from analogue experiments (e.g, Zwaan and Schreurs, 2020, 2023).

Despite the numerous insights obtained from both numerical and

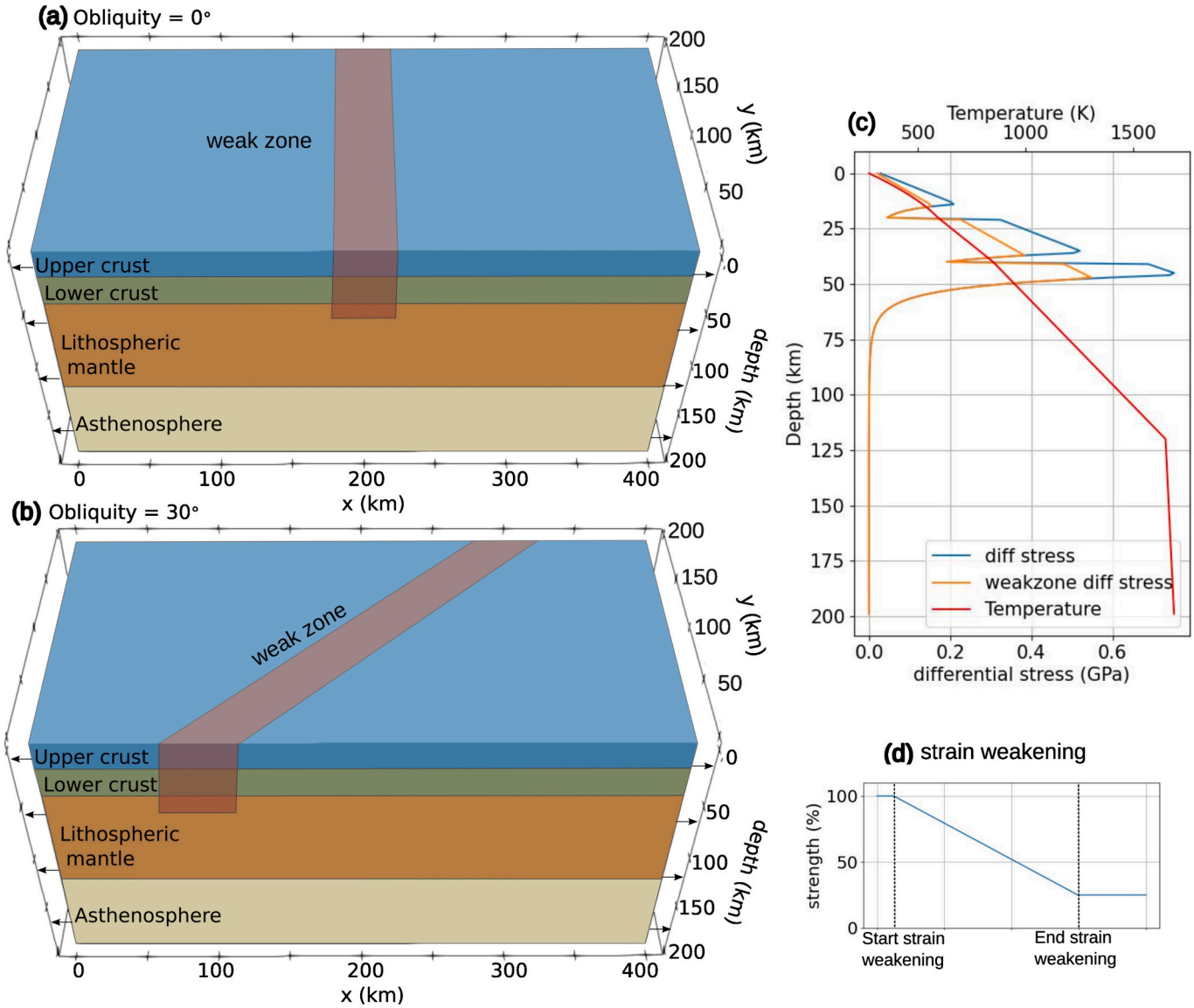

Fig. 2. Model setups of the (a) orthogonal and (b) oblique rift with upper crust, lower, crust, lithospheric mantle, and asthenosphere. The red dashed zone is the region of pre-existing weak zone. The arrow indicates the extension direction. (c) thermal gradient and strength envelopes for the Earth material (blue) and weak zone (orange). The strength profile is calculated based on Anderson fault theory (Anderson, 1905) with a strain rate of 8×10^{-17} s^{-1}. The weak zone strength is based on the average of the randomly distributed pre-existing plastic strain, equivalent to lower cohesion and internal friction angle. (d) plot showing the plastic strain weakening. (For interpretation of the references to colour in this figure legend, the reader is referred to the web version of this article.).

analogue models of rift zones undergoing varying degrees of rifting, several questions remain unanswered regarding the obliquity and the role of strength variations in regional-scale pre-existing weak zones in controlling the style of oblique rifting and fault system evolution. Particularly, the parameter space of relative weak zone strength and obliquity has not been fully explored. For example, how weak is "weak," and to what extent can it influence the shape of individual rift segments? Additionally, can different combinations of weak zone obliquity and strength promote or discourage rift segmentation? To investigate this, we use 3D geodynamic models with implemented pre-existing weak zones at an oblique angle to the divergence direction. Herein, we (1) quantify the impact of different rift obliquities on the development of rift faults and segmentation, (2) examine the role of relative weak zone strength on rift segmentation, and (3) quantify the different responses of border faults and intrarift faults to various styles of oblique rifting using fault statistical analysis as a post-processes of geodynamic modeling.

2. Methods

2.1. Geodynamic model

ASPECT is an open-source (aspect.geodynamics.org), parallel code using the finite element method to solve the coupled Boussinesq equations of momentum, mass, and energy for a Eulerian compositional field with a free-surface (Gassmöller et al., 2018; Heister et al., 2017; Kronbichler et al., 2012; Rose et al., 2017):

$$-\nabla\cdot(2\eta\dot{\varepsilon})+\nabla P=\rho g \tag{1}$$

$$\nabla\cdot u=0 \tag{2}$$

$$\overline{\rho}C_p\left(\frac{\partial T}{\partial t}+u\cdot\nabla T\right)-\nabla\cdot k\nabla T=\overline{\rho}H+(2\eta\dot{\varepsilon}):\dot{\varepsilon}-\alpha\rho Tu\cdot g \tag{3}$$

where Eq. 1 corresponds to the conservation of momentum with effective viscosity η, deviatoric strain rate tensor $\dot{\varepsilon}$, velocity u, pressure P, density ρ, and gravity g. Mass conservation is given by Eq. 2 and Eq. 3 describes the energy conservation that includes radiogenic heating H, shear/frictional heating, and adiabatic heating, with reference adiabatic density $\overline{\rho}$, heat capacity C_p, temperature T, and thermal expansivity α.

Rock types and time-dependent quantities including initial plastic strain, and non-initial plastic strain are tracked using compositional fields. Advection (Eq. 4) is solved in each of the compositional fields c_i of the model with reaction rate q_i for plastic strain and viscous strain field as below:

$$\frac{\partial c_i}{\partial t}+u\cdot\nabla c_i=q_i \tag{4}$$

The geodynamic model adopts a viscoplastic rheology (Glerum et al., 2018), combining viscous flow following the dislocation and diffusion creep function (Eq. 5) and plastic regime following the Drucker-Prager yield criterion (Eq. 6; Davis and Selvadurai, 2002)

$$\eta_{eff}^{viscous}=0.5A^{-1/n}d^{m}\dot{\varepsilon}_e^{1/n-1}exp\left(\frac{E+PV}{nRT}\right) \tag{5}$$

$$\eta_{eff}^{plastic}=\frac{3Ccos(\phi)}{\sqrt{3}\dot{\varepsilon}_e(3-sin(\phi))}+\frac{3Psin(\phi)}{\sqrt{3}\dot{\varepsilon}_e(3-sin(\phi))} \tag{6}$$

where A is a scalar prefactor, d the grain size, E the activation energy, V the activation volume, R the gas constant, n the stress exponent, m the grain size exponent, $\dot{\varepsilon}_e$ the square root of second invariant of the deviatoric strain rate, C the cohesion, and Φ the internal angle of friction. To simulate plastic strain weakening, the cohesion (C) and angle of friction (Φ) is weakened linearly by 75% from accumulated plastic strain of 0.5 to 6 (Fig. 2d). The strain healing is implemented with temperature dependence after Fuchs and Becker (2021). All these parameters are provided in Table 1 and the weak zone obliquity and strength are shown in Table 2.

Table 1
Input parameters of geodynamic model.

	unit	upper crust	lower crust	lithospheric mantle	asthenosphere
thickness	km	20	20	80	80
thermal expansivity (α)	K^{-1}	2.70E-05	2.70E-05	3.10E-05	3.10E-05
reference density (ρ0)	kg m^{-3}	2700	2850	3280	3300
thermal diffusivity (κ)	m^2 s^{-1}	7.72E-07	7.31E-07	8.38E-07	8.33E-07
heat capacity (Cp)	J kg^{-1} k^{-1}	1200	1200	1200	1200
heat production (H)	Wm^{-3}	1.50E-06	2.00E-07	0	0
Reference T (T0)	K	293	293	293	293
thermal conductivity	W m^{-1} K^{-1}	2.5	2.5	2.5	2.5
dislocation creep parameters					
power law exponent (n)	–	4	3	3.5	3.5
coefficient prefactor (A)	Pa^n s^{-1}	8.57E-28	7.13E-18	6.52E-16	6.52E-16
activation volume (V)	m^3 mol^{-1}	0	3.80E-05	1.80E-05	1.80E-05
Activation Energy (Q)	J mol^{-1}	2.23E+05	3.45E+05	5.30E+05	5.30E+05
diffusion creep parameters					
power law exponent (n)	–	1	1	1	1
grain size exponent (m)		2	3	0	
coefficient prefactor (A)	Pa^n s^{-1}	5.97E-19	2.99E-25	2.25E-09	2.25E-09
activation volume (V)	m^3 mol^{-1}	0	3.80E-05	6.00E-06	6.00E-06
Activation Energy (Q)	J mol^{-1}	2.23E+05	1.59E+05	3.75E+05	3.75E+05
grain size (d)	m	1.00E-03	1.00E-03	1.00E-03	1.00E-03
surface heat flow	W m^{-2}	0.055	0.035	0.03	0
Cohesion (C)	Pa	2.00E+07	2.00E+07	2.00E+07	2.00E+07
Frication angle (Φ)	degree	20	20	20	20

Table 2
Name of models (bold) and weak zone strength and obliquity used in all figures.

Maximum weak zone plastic strength	0°	15°	30°	45°	60°
1.6	Fig. 9 (**C1R5**)	Fig. 9 (**C1R4**)	Fig. 9 (**C1R3**)	Fig. 9 (**C1R2**)	
2	Fig. 9 (**C2R5**)	Fig. 9 (**C2R4**)	Fig. 9 (**C2R3**)	Fig. 9 (**C2R2**) Fig. 6I	Fig. 9 (**C1R1**)
2.2				Fig. 4A&E (**EA45**) Fig. 7I	
2.4				Fig. 4B&F (**EB45**)	
2.6	Fig. 9 (**C3R5**) Fig. 6A Fig. 7A	Fig. 9 (**C3R4**) Fig. 3A&E Fig. 6B Fig. 7B Fig. 5(G-L)	Fig. 9 (**C3R3**) Fig. 3B&F Fig. 6C Fig. 7C	Fig. 9 (**C3R2**) Fig. 3C&G Fig. 4C&G Fig. 6D Fig. 6H Fig. 7D Fig. 7H	Fig. 9 (**C2R1**) Fig. 3D&H Fig. 6E Fig. 7E
2.8				Fig. 4D&H (**EC45**) Fig. 5(A-F)	
3	Fig. 9 (**C4R5**)	Fig. 9 (**C4R4**)	Fig. 9 (**C4R3**)	Fig. 9 (**C4R2**) Fig. 6G Fig. 7G	Fig. 9 (**C3R1**)
4	Fig. 9 (**C5R5**)	Fig. 9 (**C5R4**)	Fig. 9 (**C5R3**)	Fig. 9 (**C5R2**) Fig. 6F Fig. 7F	Fig. 9 (**C4R1**)
5		Fig. 9 (**C6R4**)	Fig. 9 (**C6R3**)	Fig. 9 (**C6R3**)	
6	Fig. 9 (**C6R5**)				Fig. 9 (**C5R1**)
7					Fig. 9 (**C6R1**)

2.2. Model setup

Our 3D model is a 400 × 200 × 200 km box with 20-km-thick upper and 20-km-thick lower crustal layers using a dry quartzite and wet anorthite rheology, respectively. We use a 80-km-thick lithospheric mantle and a 80-km-thick asthenosphere of dry olivine (Fig. 2). Our selected lithosphere thickness is comparable to that of East Africa (Pasyanos et al., 2014). The model mesh features a resolution gradually decreasing from the top of the model to the bottom. This resolution corresponds to discrete layers with resolutions of diminishing from 1.25 km, to 2.5 km, to 5 km, and finally to 10 km at depths of 10 km, 30 km, 50 km, and beyond.

The initial temperature in the model is prescribed using a steady-state geotherm (Chapman, 1986) from surface to the lithosphere–asthenosphere boundary (LAB) with a Moho, LAB, and mantle potential temperature of 576 °C, 1376 °C, and 1316 °C, respectively. From LAB to the bottom of the domain, the initial temperature distribution is determined by a mantle adiabatic gradient (0.5 K/km). All other boundaries are set to zero heat-flux. The right and left boundaries are a free slip surface, extended with a total extension rate of 5 mm/yr for 10 Myr. The top boundary is a free surface and outflow at the right and left edges of the model is compensated by inflow at the bottom boundary to conserve volume.

To implement a pre-existing weak zone, numerical modeling studies either prescribe a local thermal anomaly (Brune et al., 2017a, 2017b; Corti et al., 2003; Glerum et al., 2020; Neuharth et al., 2022) and/or a single weak seed or a prescribed fault (e.g., Olive et al., 2022). Some models also incorporate a random distribution of pre-existing plastic strain to define a region of weakness (Duclaux et al., 2020; Naliboff et al., 2020; Richter et al., 2021). Herein we adopted the later approach and define a 40-km-wide (similar to previous weak zone width, e.g. Brune, 2014) and 80-km-deep zone with a randomized initial plastic strain. The weak zones are delineated by regions with higher initial plastic strain compared to the surrounding rocks, producing a yield strength profile that allows for rock failure to occur at relative lower stresses (Fig. 2). The magnitude of strain within the weak zone gradually decreases from the center towards the edge, following sinusoidal curves, representing suture zones or paleo rifts within the brittle portion of the lithosphere (Fig. 2). The tapered weak zone involves a gradual transition between the weak zone and normal crust without a focusing effect. The mean strength of the weak zone is also shown in Fig. 2c and can be varied by changing the maximum plastic strain of the weak zone. Therefore, the obliquity of the rift is reflected by the angle between the axis of this weak zone and *E*-W divergence direction, from 0° to 75° with intervals of 15°. Meanwhile, we examine the role of weak zone strength by varying the maximum weak zone plastic strain from 1.5 to 6, representing the range of relative strength of weak zones compared to surrounding rock with zero plastic strain.

2.3. Fault statistic analysis

To quantify strain localization during oblique rifting, fault analysis is carried out using an open-source (github.com/thilowrona/fatbox) image processing toolbox called Fatbox (Wrona et al., 2022). We track fault development and quantify the total number of faults, fault lengths, azimuths, and their displacement. Fatbox can use model outputs of strain rate, cumulative strain, or topographic data in 2D and extract connected nodes as faults (details in Neuharth et al., 2022; Wrona et al., 2022). The fault displacement can be estimated as the relative movement of nodes projected on a fault between two time steps. Here we extract faults using topography data at 10 Myr and for each fault longer than 2500 m, we calculate their azimuth and throw for statistical analysis. Notably, the azimuth of fault is the orientation of the 1D fault on topography ranging from -90° to 90° and the length and throw of the fault is also measured on topography. Moreover, the faults caused by edge effects (within 10 km of the edges and outside of weak zone) are filtered out to avoid their effects on the fault statistical analysis.

In this study, certain processes of rifting are excluded in our models. First, we do not consider melting and associated magma migrations, intrusions, dykes, and magma chamber formations. By restricting the model runtime to early stages of rifting, the influence of magmatism is due to decompressive melting would be minimal. Second, to ensure that we can isolate the effects of pre-existing weak zones, we exclude the impact of surface processes on rift evolution in our numerical experiments. (e.g., Neuharth et al., 2022; Olive et al., 2022; Wolf et al., 2022). However, it's worth noting that previous studies (e.g., Zwaan et al., 2018) have indicated that surface processes are not the primary controlling factor in early-stage rift structural evolution. Last, we do not explore the parameter space of crust and mantle rheology in this study, as these aspects have been thoroughly investigated in prior analogue and numerical modeling efforts (e.g., Brune, 2014; Duclaux et al., 2020; Naliboff et al., 2020; Zwaan et al., 2022). Instead, we focus on the

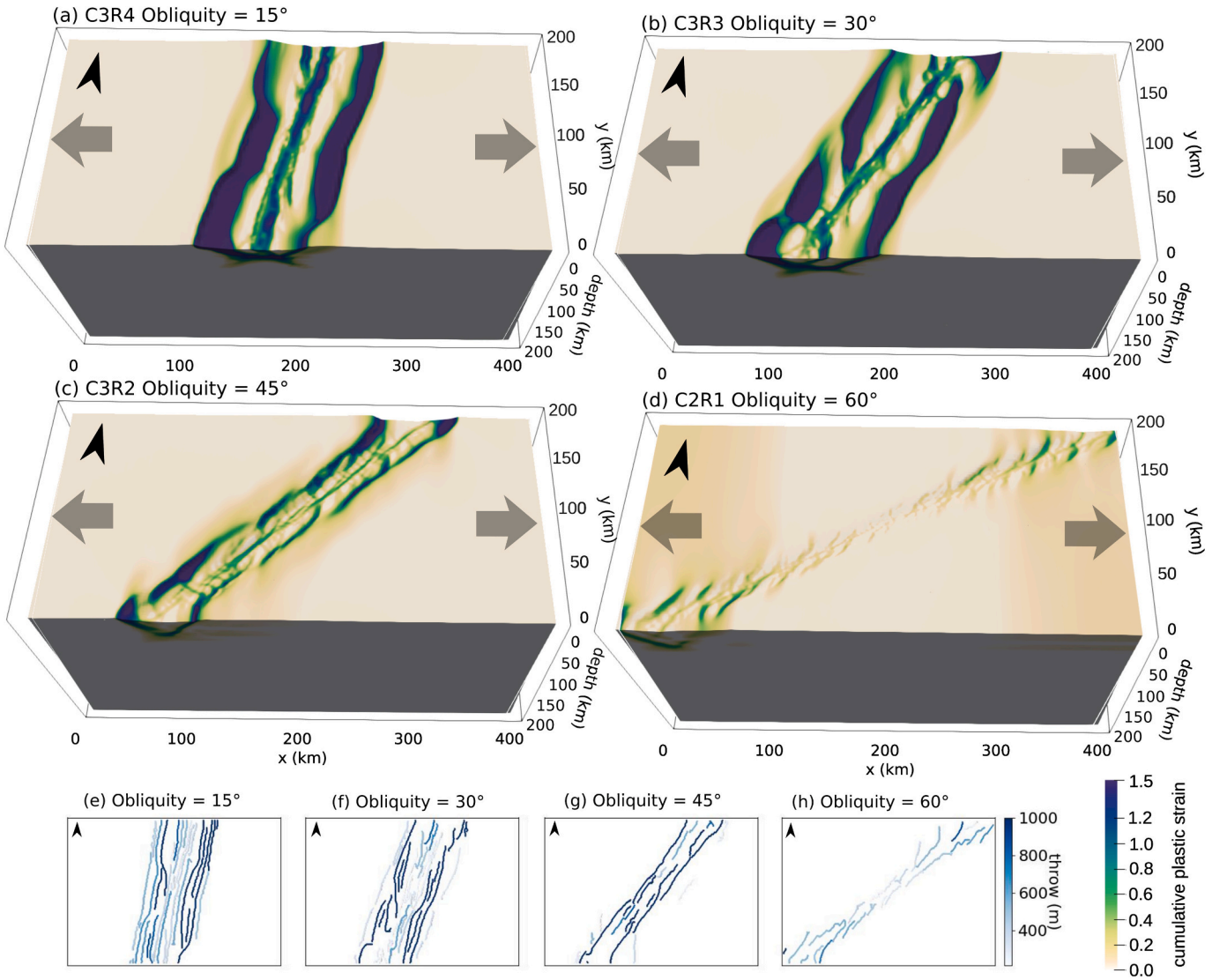

Fig. 3. Cumulative plastic strain for models with obliquity of (a) 0°, (b) 15°, (c) 30°, and (d) 45° after 10 Myr. The cumulative plastic strain delineates the fault system. The gray arrows indicate divergence direction. (e-h) Extracted faults from topography data for (e) 0°, (f) 15°, (g) 30°, and (h) 45° on the same scale. The strength of pre-existing weak zone is with the same maximum plastic strain(2.6). Details on the weak zone strength and obliquity is shown in Table 2.

relative strength and obliquity of the pre-existing weak zone.

3. Results

Our model results demonstrate the influence of oblique weak zones by (1) describing the rift evolution and associated fault development in response to different obliquities over 10 Myr, (2) evaluating the effect of relative strength of the weak zone on strain localization, and (3) statistical analysis of different fault geometries due to oblique rifting.

3.1. The role of rift obliquity

In our models, rifting initiates with the emergence of small-scale strain localization in the pre-existing weak zone during extension. With progressive stretching, these initially dispersed minor faults amalgamate into a select number of significant faults, each characterized by distinct patterns correlating with varying degrees of obliquity. For rifts with an obliquity of *15°*(Fig. 3a*, model C3R4*) and a medium weak zone strength (plastic strain of 2.6, applied to all cases evaluating weak zone obliquity in this section), fault coalescence gives rise to the rapid development of border faults over 2–3 Myr synchronous with mantle upwelling and lithospheric thinning in the rift zone. The border faults crosscut the entire model domain from north to south in the upper crust, forming a single continuous rift segment. Border faults accommodate majority of the strain throughout the 10 Myr model run, with some strain localization near the rift basin center generating a graben-in-graben structure (Fig. 3a). The resulting rift at 10 Myr is ~90 km wide and forms the widest rift basin in comparison to other model results, because the stress is purely extensional over the entire model run.

For an obliquity of 30°, an en-echelon rift geometry starts to develop, comprising a set of subparallel, closely-spaced, overlapping low-strain faults staggered in such a way that the evolving plate boundary runs obliquely to the strike of the individual faults (see the example in Fig. 1f). The en-echelon structure first forms across the rift basin at ~ 3 Myr prior to rift segmentation. These small-scale en-echelon structures then coalesce to form the rift border faults. Instead of the long and continuous border faults observed for the orthogonal rifts, separate border faults form as multiple rift segments (Fig. 3b, model C3R3). Distinct intrarift faults striking perpendicular to the divergence direction develop from ~ 5–10 Myr.

When the obliquity is 45° (Fig. 3C, model C3R2), rift evolution is much slower with less mantle upwelling, and comparatively limited

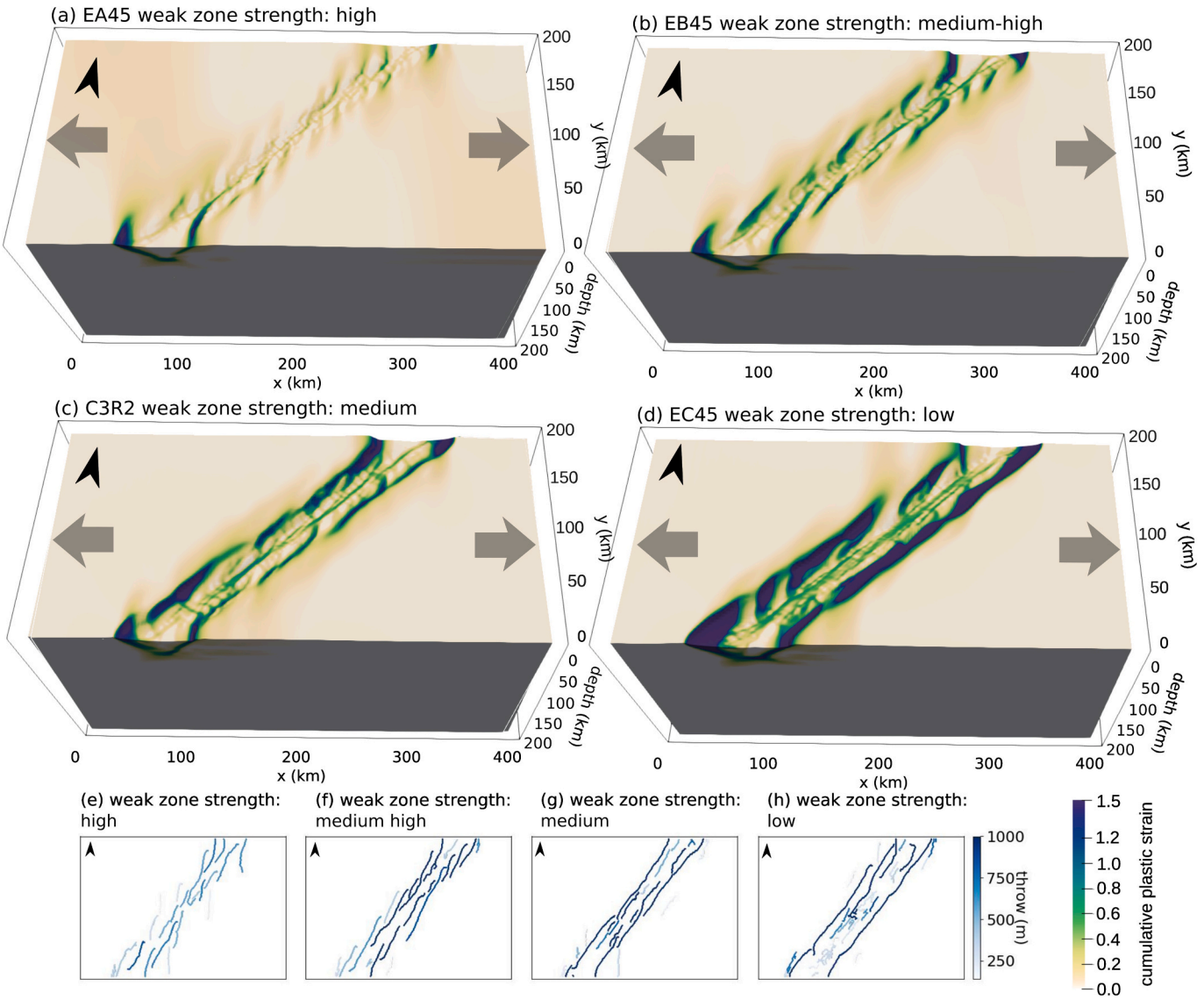

Fig. 4. Cumulative plastic strain for models with different weak zone strengths of (a) high, (b) medium high, (c) medium, and (d) low with a fixed obliquity of 45°. The gray arrows indicate divergence direction. The cumulative plastic strain delineates the fault system. (e-h) Extracted faults from topography data with different maximum plastic strain. Details on the weak zone strength and obliquity is shown in Table 2.

extension, strain localization and fault system migration. In these models, the en-echelon structure develops within a narrower rift basin (~30–50 km), with shorter lengths and lower strain compared to the low/moderate obliquity models. These en-echelon structures persist over 10 Myr with constituent faults exhibiting strikes that are generally perpendicular to the divergence direction (Fig. 3c).

With high obliquity (60°, Fig. 3d, model C2R1), the en-echelon structures are dominant throughout the domain. While, the throw in the center of the domain is much smaller compared to that of other models, showing a transforming to a strike-slip system. As a result, the rift basin is characterized by a narrow and less developed rift zone with no distinguishable border faults and comparatively less lithospheric thinning (Fig. 3d).

3.2. Role of weak zone strength

The relative strength of a pre-existing weak zone also plays a major role in rift evolution. To demonstrate this, we vary the weak zone strength from high to low relative to background with a fixed obliquity of 45° (Fig. 4). We find that for a relatively strong weak zone, strain localization is evenly partitioned across rift basin and is represented by en-echelon structure comprising of faults with minimal throw (Figs. 4a & 4e, model EA45). Moreover, lithospheric thinning and accompanied mantle upwelling is distributed across the entire domain due to the widely diffused viscous strain in the lithosphere.

When the weak zone strength is intermediate (model C3R2), the en-echelon structure becomes inactive at ~5 Myr (Fig. 5) as strain begins to migrate to the border faults. Rift basin segmentation is established by ~6 Myr and strain is preferentially localized on the border faults by 10 Myr. While the border faults nucleate parallel to the pre-existing weak zone, tips of the intrarift faults remain (sub)orthogonal to the divergence direction throughout model time (Figs. 4b,c, see also Section 3.3).

Systems with especially low weak zone strength, however, promote rapid coalescence of rift faults at early stages of rift evolution. The early phase of en-echelon structure development ends at 3 Myr and strain then starts to migrate to the border faults, resulting in two border faults that cut through the entire domain (Fig. 4d). This progression is similar to orthogonal rifts with a stronger weak zone (Fig. 3a and b, initial strain of 2.6 vs 2.8). The development of border faults with high accumulated strain (with throw >1 km, Fig. 4h) is also accompanied by greater

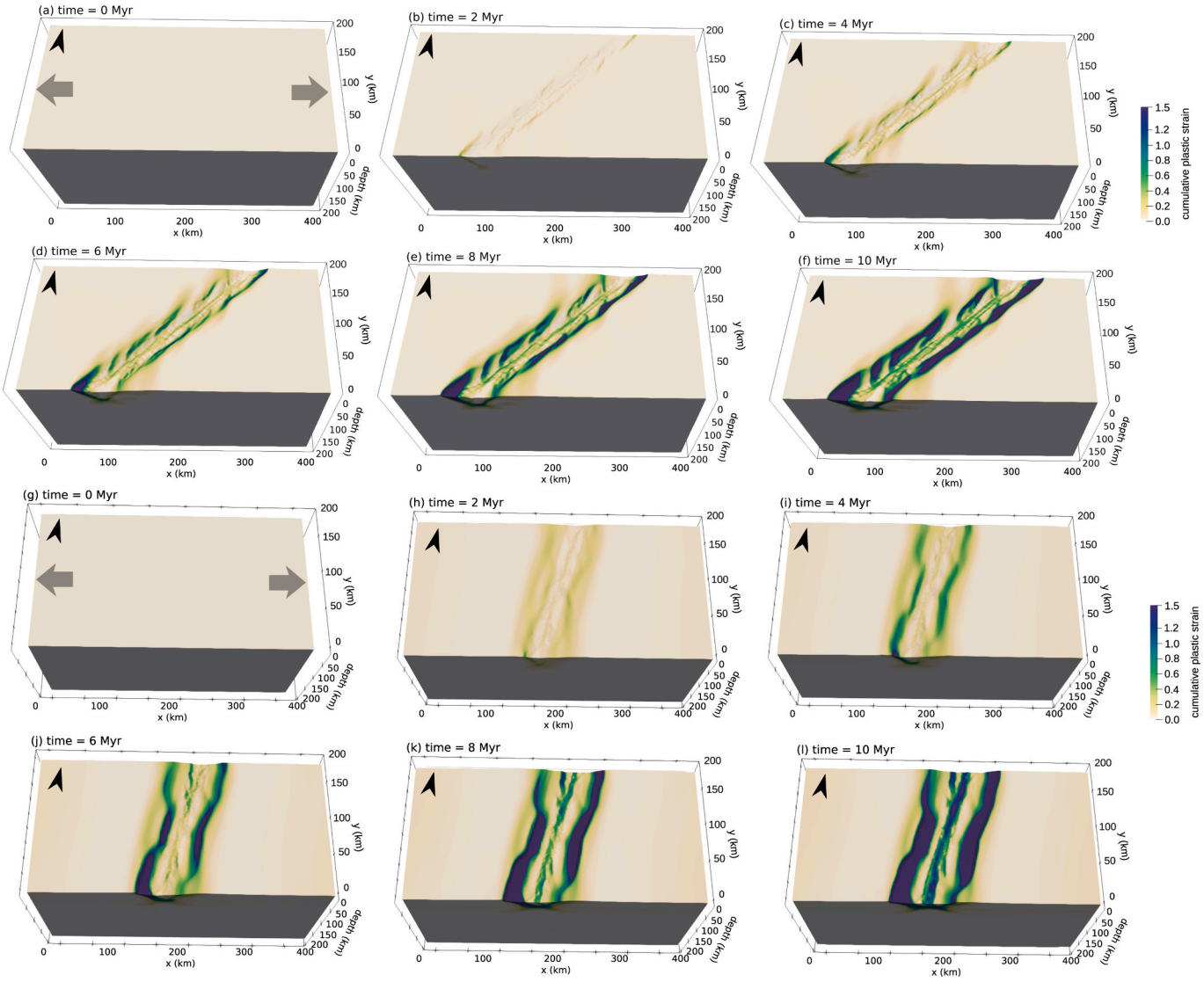

Fig. 5. Cumulative strain localization from 0 to 10 Myr, showing the structural evolution of a rift with a obliquity of 45°(EC45, a-f) and 15°(C3R4, g-l) weak zone with a step of 2 Myr.

asthenospheric upwelling and lithospheric thinning (necking phase of rifting) compared to rifts with a stronger weak zone (Fig. 4d, model EC45).

3.3. Statistical analysis of faults

To quantify the patterns of strain localization, we use Fatbox to extract faults from the modeled results to examine the azimuth, throw, and length of fault networks at 10 Myr. From this, we note that the fault azimuth distribution is clearly influenced by weak zone obliquity (Fig. 6). When the obliquity is low (*0*°), the azimuth distribution exhibits a peak frequency at ~0°, indicating that all border and intrarift faults strike perpendicular to the divergence direction (Fig. 6a). As obliquity increases, we observe a multimodal distribution of faults azimuth (Figs. 6c-e), highlighting the different patterns of strain localization throughout rift basin. The pattern suggests that border faults tend to strike parallel to the weak zone axis and intrarift faults preferentially strike perpendicular to the divergence direction (i.e. azimuth 0°, Figs. 6c-e). The different orientations observed between border and intrarift faults are also shown in map-view in Figs. 3g-h and Figs. 4e-f.

Furthermore, the relative strength of the weak zone is also shown to affect fault azimuth distribution when the obliquity is fixed at 45°. A bimodal pattern in fault azimuth exists for high and medium strength weak zones reflecting the development of both intrarift and border faults with different orientations, here 0° and 45°, respectively (Figs. 6h-i). In contrast, when the weak zone strength is low, fewer intrarift faults develop, and few, if any, are oriented parallel to the weak zone axis (Figs. 6f-g).

Fault throw maps (Figs. 3, 4) and histograms (Fig. 7) can also provide insights into strain localization during oblique rifting. Consistent with our results above, an increase of obliquity promotes a transition from preferential development of border faults with large throws to en-echelon structures with medium to small throws (Figs. 3e-h & 7). Similarly, we find a decrease of fault throw, from a maximum of 2000 m to 500 m, for low to high obliquity rifts, respectively (Figs. 7a-e). In contrast, a decrease of weak zone strength promotes higher throws on border faults (Figs. 4e-h, 7f-i).

We also notice that weak zone obliquity plays an important role in rift fault lengths during extension. We observe that multiple rift faults with shorter lengths develop in rifts with either high obliquity (Fig. 3c) or medium weak zone strength (Fig. 4 b& c). Moreover, low obliquity results in the formation of rift faults with longer lengths regardless of

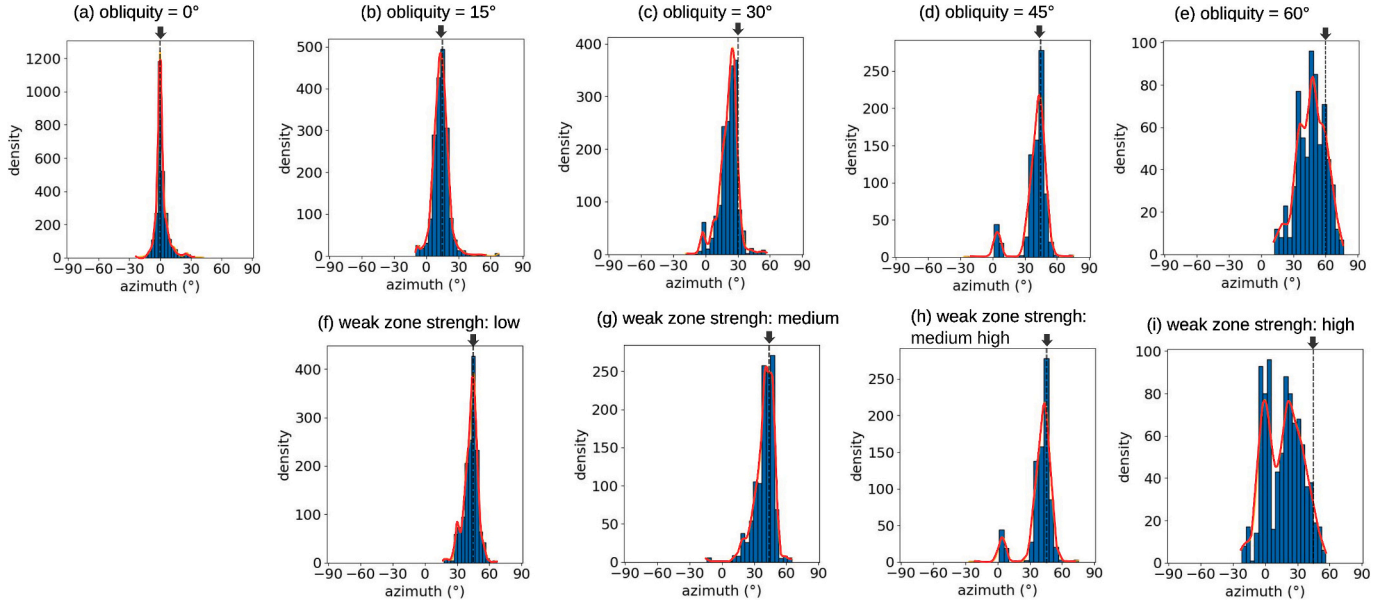

Fig. 6. Histogram (blue) and Kernel distribution estimation (red) plot of fault azimuths with different obliquities (first row) and pre-existing weak zone strengths (second row). The black dash-line and arrow indicate the weak zone obliquity. Details on the weak zone strength and obliquity is shown in Table 2.

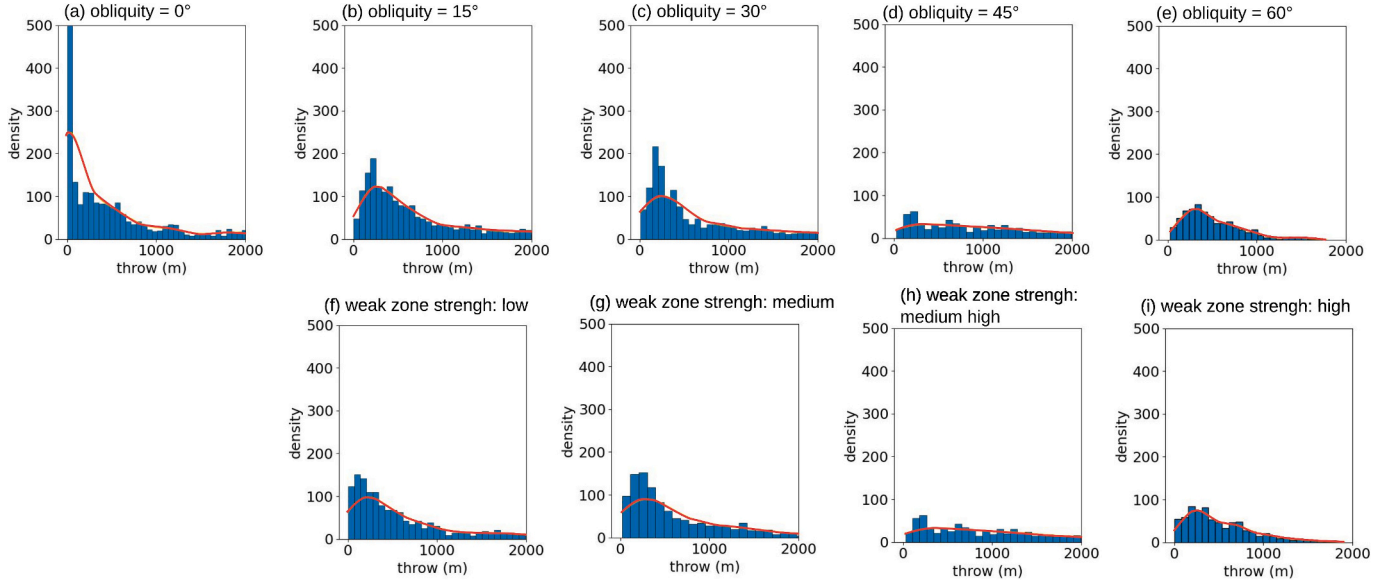

Fig. 7. Histogram (blue) and Kernel distribution estimation (red) plot of fault throws for different obliquity (first row) and pre-existing weak zone strength (second row). The fault throw data on the second row is from models with different maximum plastic strain. Details on the weak zone strength and obliquity is shown in Table 2.

weak zone strength (Figs. 3, 4, & 8b). This relationship between rift obliquity and fault length is illustrated in Fig. 8a, where the normalized rift fault length (each fault's length normalized to the length of the rift axis) depicts a negative correlation with rift obliquity. Our modeling results offer new insights into structural evolution of oblique rifts, revealing that it is influenced not only by the weak zone obliquity but also by its relative strength. To illustrate these findings, we have created Fig. 9 as a summary of our modeled results. This figure encapsulates the key trends and variations observed in our study, providing a visual representation of how different combinations of obliquity and strength affect rift segmentation.

4. Discussion

4.1. Effect of weak zone obliquity and strength on rift evolution

We find that the nature of strain localization is strongly modified by pre-existing weak zone obliquity, consistent with previous numerical and analogue studies (e.g., Brune, 2014; Duclaux et al., 2020). Previous numerical studies suggested there are three key phases of oblique rifting regarding the timing of strain localization (Brune, *2014*; Duclaux et al., *2020*). The initial phase 1 starts with fault coalescence as strain localizes on faults formed from widely distributed deformation within the pre-existing weak zone. Rift phase 2 involves the development of en-echelon structures featuring a broad distribution of fault orientations, before strain successively localizes on rift-parallel faults during

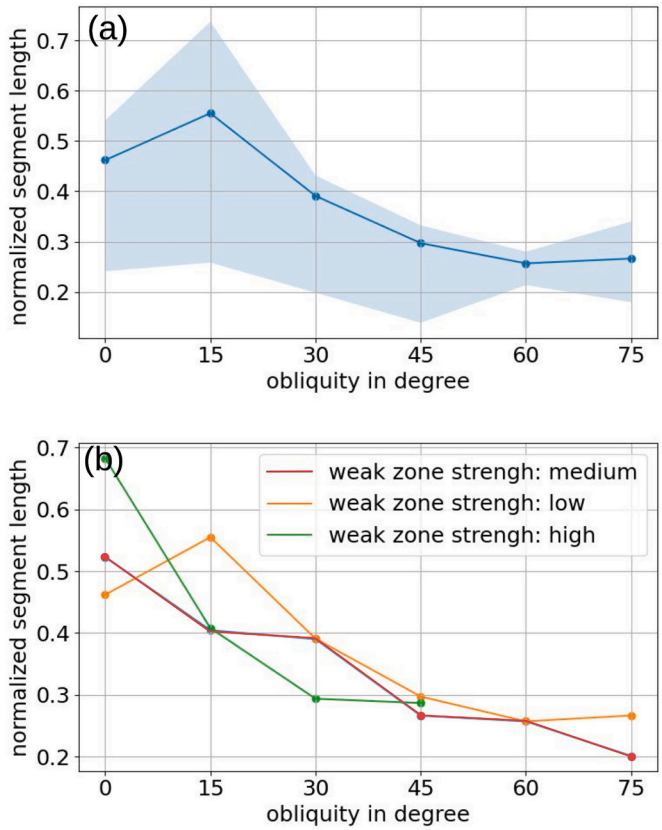

Fig. 8. (a) Plot of normalized segment length (the ratio between segment length and rift axis length) for different rift obliquities with medium weak zone strength (2.6). The blue shaded region represents the uncertainty with 75% confidence. (b) Plot of normalized segment length for different strengths of weak zone.

extension. During this stage, necking-induced density variations and strain partitioning between border faults and intrarift faults result in preferential strain accommodation on rift-parallel faults. Finally, phase 3 involves pre-breakup strain localization that rapidly terminates the previous phase (en-echelon), resulting in the linkage of previous rift segments with strain localizing on faults striking (sub)perpendicular to the divergence direction.

Similar to these previous studies, we observe the development of en-echelon structures in oblique rifts during the initial rift stages for medium and high rift obliquities (Fig. 3); however, the timing and pattern of faulting and rift segmentation differs from the models of Brune (*2014*) and Duclaux et al. (*2020*), particularly when the strength of the weak zone is considered. First, at low rift obliquity (0° to 15°), strain localizes along the rift-axis with rift-perpendicular border faults and intrarift faults forming immediately, without the rift experiencing a phase of en-echelon structure formation. This is likely due to border fault and intrarift faults rapidly accommodating dip-slip deformation during (sub) orthogonal rifting (Figs. 3e-f). Second, instead of early-stage strain migration into the rift valley, we find that strain can localize at the rift border faults for long periods before the lithospheric necking phase (Figs. 3, 4). These long-lived border faults preferentially form under either condition of low obliquity or low weak zone strength. When the weak zone strength is low, the distinct cohesion difference promotes strain localization at the contact between the weak zone and surrounding intact lithosphere, forming highly pronounced border faults. The lithospheric necking and subsequent continental breakup would likely and preferentially occur from such border faults. Therefore, to reproduce the three-phase oblique rift evolution style and form the classic en-echelon structures (e.g., Brune, *2014*, Figs. 3d, 4a), both medium-high obliquity (> 30°) and a relatively high strength (high and medium-high in Fig. 4) of the weak zone is required. This suggests that the en-echelon structure is not necessarily a distinct phase of oblique rift systems (i.e., phase 2 mentioned above). These results reveal that relative strength of lithospheric-scale weak zones, *and* not just their orientation, plays a critical role in rift evolution.

Our results corroborate and expand upon previous analogue experiments on the role of weak zone obliquity. For example, Agostini et al.

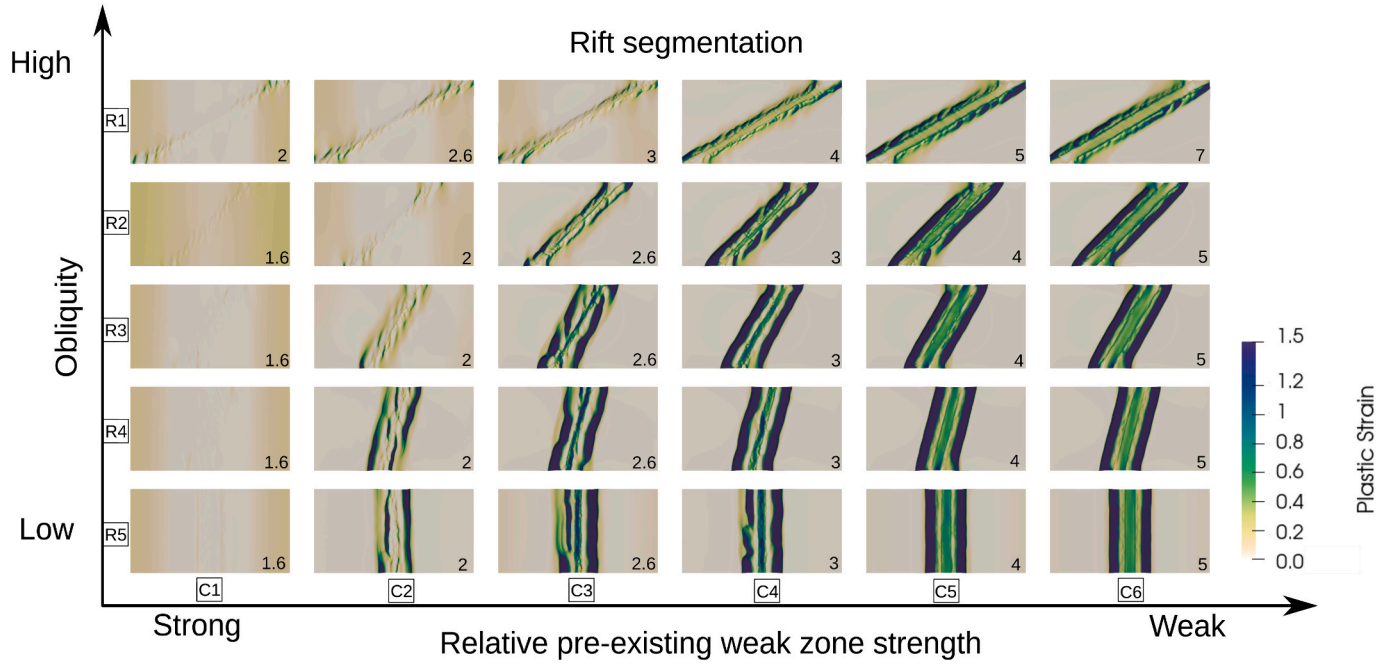

Fig. 9. Matrix plot of modeled results between obliquity (y axis) and relative weak zone strength (x axis). All the modeled results are at time of 10 Myr all with the same setup but variable obliquity and weak zone strength. The plastic strain shown for different models are at the same scale. Details on the weak zone strength and obliquity is shown in Table 2. The inset number shows the maximum plastic strain of the initial weak zone.

(2009) demonstrated with analogue modeling of oblique extension that border faults form via coalescence of multiple small-scale faults that initially form perpendicular to *divergence* direction. Our model results suggest that the rift-axis parallel border faults can be formed due to either low weak zone strength (Figs. 4c,d), or from fault coalescence under low obliquity conditions (Figs. 3a,b). Therefore, both the relative strength of the weak zone and rift obliquity contribute to the appearance of rift-axis parallel border faults.

Our statistical fault analysis also agree with results from previous analogue studies. Statistical analysis of rift faults by Clifton et al. (2000) suggested that the fault lengths at the 95th percentile decrease with increase in rift obliquity. Similarly, Agostini et al. (2009) also found that the mean length of rift faults decreases as obliquity increases from 0° to 60°. Faults in our model also exhibit similar geometric patterns, where higher obliquity leads to smaller fault lengths (Fig. 8a) as strain is more widely distributed in high obliquity rifts. Moreover, the different orientations between intrarift faults and border faults under oblique rifting is also reported by previous analogue models (e.g., Corti et al., 2013; Philippon et al., 2015; Osagiede et al., 2021), where intrarift faults are mostly perpendicular to divergence direction and border faults parallel to the rift axis and the weak zone. Furthermore, o*ur results of variation of rift width* vs *obliquity are also supported by previous analogue experiments that indicate decreasing rift width with increasing rift/divergence obliquity (*Zwaan et al., 2016*)*.

Our modeling results quantify the critical role of pre-existing weak zone strength in rift evolution. Multiple studies have reported that the existence of weak zones in the lithosphere may control rift basin architecture and segmentation (e.g., Ethiopia and Kenya, Corti et al., 2022; Malawi Rift, Laó-Dávila et al., 2015; Rhine Graben, Grimmer et al., 2017; Lower Shire Graben, Kolawole et al., 2022). Morley et al. (2004) reported that the strength of pre-existing structures with respect to each other and to the strength of intact host rock is one of the key factors that influences oblique extensional systems. Our results suggest that differences in weak zone strength can lead to distinct faulting patterns and segmentation (Fig. 4). The analysis of fault statistics reveals that strain preferentially localizes along border faults when weak zone strength is low. We attribute this to the larger and abrupt rheological changes at lithospheric boundaries where these border faults form (Fig. 6). Furthermore, rift systems transition from distributed to localized extension at a much faster rate when the relative strength of weak zones is low.

Our modeling results provide new insights on rift segmentation, which is related to not only the weak zone obliquity, but also its relative strength. Rift segmentation is characterized by partitioning of strain localization and can reflect the weak zone geometry (e.g., Muirhead et al., 2019; Nixon et al., 2016). When the pre-existing weak zone is strong, it is less likely that the weak zone will be reactivated to form typical rift border faults (left columns of Fig. 9, C1-C3), thus increasing the likelihood of en-echelon structures with low relief within the weak zone. On the other hand, when the weak zone is far weaker than the surrounding bedrock, strain preferentially and rapidly localizes on the border faults (right columns of Fig. 9, C4-C6). Neither case leads to the development of multiple rift segmentation. *Strain tends to localize onto distinct rift segments when the weak zone strength falls within the spectrum defined by the two end-member scenarios. Moreover, as rift obliquity increases, a weaker weak zone becomes more critical for the segmentation. This suggests that high obliquity may foster the development of multiple rift segments, regardless of weak zone strength (*Fig. 9*)*.

4.2. Implications and insights into the evolution of natural continental rifts

Rift segmentation in natural rift examples can be complex, where the effects of obliquity, weak zone strength, and other factors can largely overprint each other. Two different rifts with similar segmentation can result from different deformation histories, and thus interpreting rift evolution using present-day the configuration of segments can be inherently ambiguous (e.g., Reeve et al., 2015; Zwaan et al., 2021). Indeed, our results demonstrate that combinations of high obliquity and low weak zone strength can develop the same rift segmentation pattern as combinations of low obliquity and high strength (Fig. 9). In general, the interplay between obliquity and weak zone strength may lead to very similar rift configurations (Fig. 9). Therefore, we suggest that detailed investigations of fault activity are needed to properly determine the structural history of complex rift systems and the cause of rift segmentation.

Temporal changes in divergence direction may also introduce complexities in interpreting rift segmentation and evolution. Analogue models have indicated diverse responses of rift structures in various layers to changes in divergence direction over time (e.g., Bonini et al., 1997; Wang et al., 2021; Zwaan et al., 2022). However, herein, we specifically concentrate on the final stages of strain localization after 10 Myr model runs and do not account for temporal variations. Our modeled results indicate that rift fault populations with distinct strikes can co-exist under one optimal obliquity without the need for a change in the divergence direction. For example, intrarift faults and border faults can develop with different orientations despite a common divergence direction (Figs. 3, 6), in alignment with the results from previous analog models (Zwaan et al., 2021). As such, when encountering such rift arrangements in the field, as for instance in the Mesozoic Northeast Atlantic and North Sea (e.g., Zwaan et al., *2024*), there is no need to invoke changes in the divergence direction over time.

In natural examples, it is challenging to quantify the mechanical strength of pre-existing weak zones that underlie natural continental rifts at a scale that is relevant for understanding their controls on rift development. However, our model results may provide insights into the development of certain natural rifts with seemingly enigmatic structural relationships with the pre-rift basement that they developed within. Our numerical model setup incorporates a pre-rift intra-basement weak zone that spans the entire scale of a rift basin (i.e., 50 km wide and 200 km long), with ~5 km-wide gradational boundaries. In the context of natural rifts, this model pre-rift structure represents large inherited orogenic terranes in the crystalline basement of continental rift environments. Examples will include the metamorphic terranes of the Ubendian Belt underlying the Rukwa Rift (e.g., Figs. 10a&b), the Mozambique Belt underlying the Kenyan Rift and Malawi Rift, the Damaran-Lufilian-Zambezi Orogen underlying the Luangwa Rift, Okavango Rift, Zambezi-Kariba Rift, and the Shire Rift Zone, all along the East African Rift System (e.g., Daly, 1988; Daly et al., 1989; Fritz et al., 2013; Sarafian et al., 2018). Other examples include the Sierra Nevada Igneous terranes hosting the Walker Lane Rift Zone and the Sevier and Central Nevada fold and thrust belts underlying the Basin and Range (e.g., Figs. 11a,b; Greene and Schweickert, 1995; Long, 2012). Furthermore, the kilometer-scale wide margins of the model weak zone is representative of terrane boundaries in the inherited basement of rift zones, examples of which include the steep ductile shear zones bounding the terranes of the Ubendian Belt (e.g., Fig. 10b; Daly, 1988; Heilman et al., 2019; Kolawole et al., 2021b), and the ductile shear zones and thrust faults bounding the Sierra Nevada terranes (e.g., Fig. 11b; Greene and Schweickert, 1995; Dunne and Walker, 2004).

Several studies have provided evidence suggesting the controls of inherited basement terrane boundaries on rift localization and rift structure (e.g., Daly et al., 1989; Wheeler and Karson, 1989; Kinabo et al., 2007; Katumwehe et al., 2015; Phillips et al., 2019; Muirhead and Kattenhorn, 2018; Heilman et al., 2019; Kolawole et al., 2021b; Kolawole et al., 2022; Shaban et al., 2023; Phillips et al., 2023). However, there is little understanding of the role of terrane-scale (i.e., 30–50 km) mechanical strength on the evolution of the rifts that develop within them. Our modeled weak zone is of basement terrane-scale, providing an opportunity to evaluate how the possible variability of inherited terrane strength may have influenced the evolution of a continental rift. Here, we consider two actively propagating rift zones: the Rukwa Rift, an

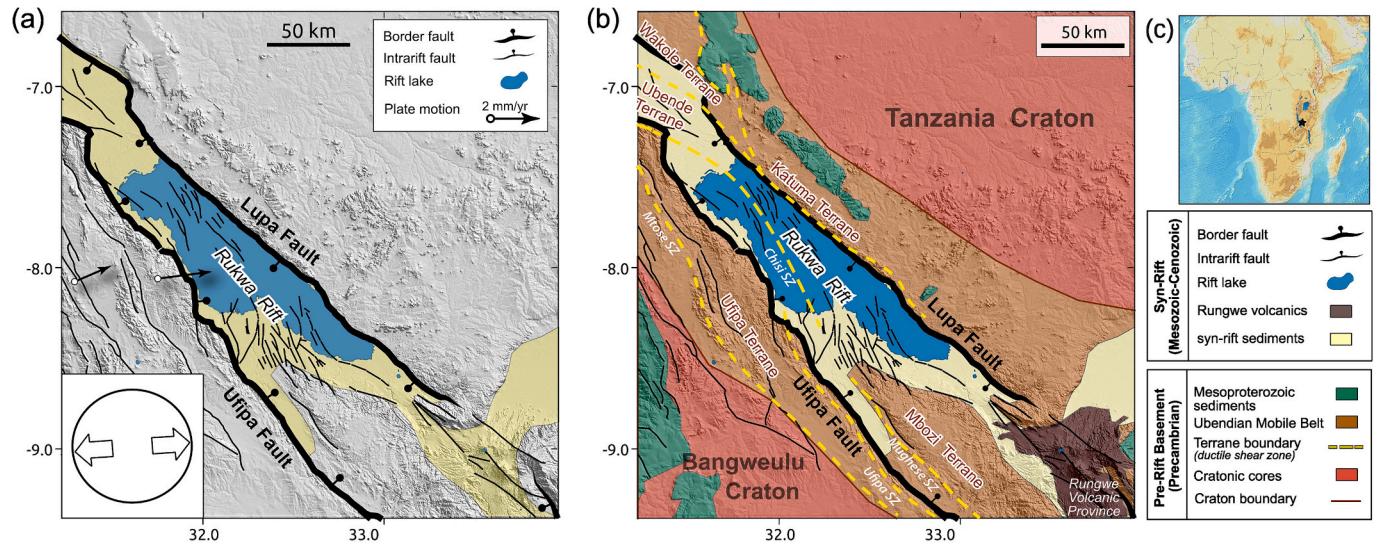

Fig. 10. (a) Topographic relief map, and (b) geologic map of the Rukwa Rift, East Africa – a zone of active low-obliquity rifting (low to medium, ~36°). Fault traces are from Morley et al. (1992, 1999), Delvaux et al. (2012), and Kolawole et al. (2021a). Basement terranes and shear zones are from Daly (1988), Daly et al. (1989), Lenoir et al. (1994), and Kolawole et al. (2021b). Geodetic plate velocity vectors (black arrows) are from Stamps et al. (2008), and white arrows represent the regional divergence direction in southern Tanganyika Rift (from Lavayssière et al., 2019). (c) Map of Africa, the star indicates the location of Rukwa Rift.

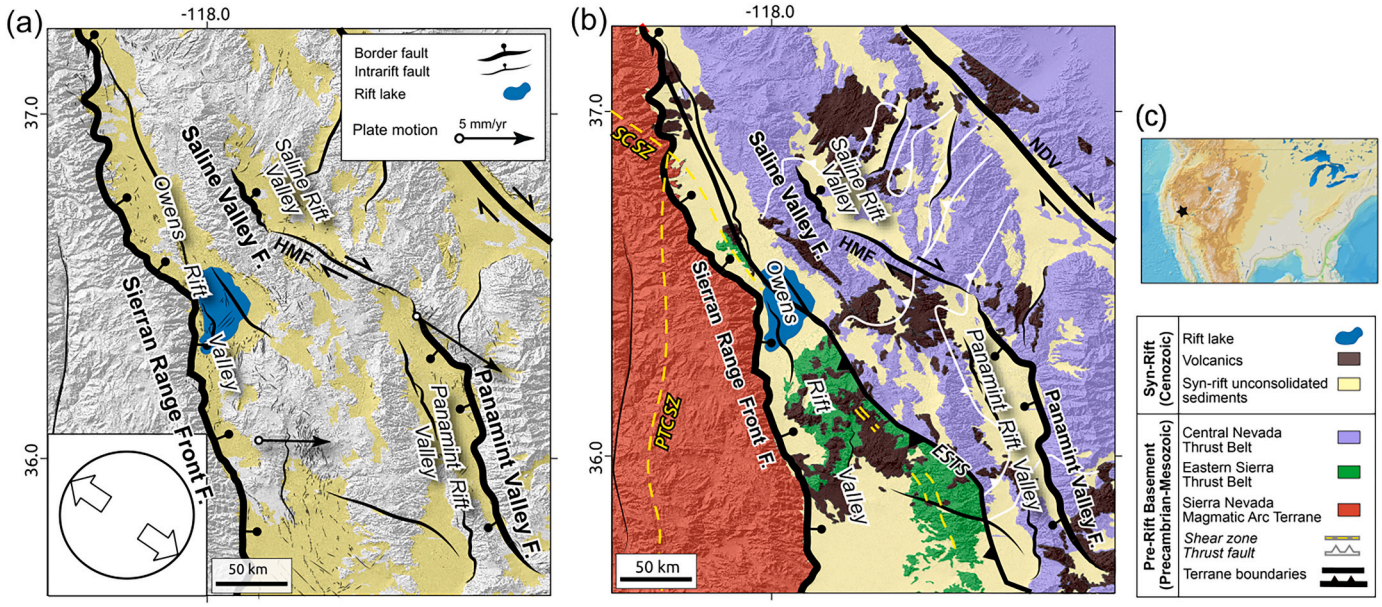

Fig. 11. (a) Topographic relief map, and (b) geologic map of the Southern Walker Lane, Eastern California – a zone of active high-obliquity rifting (medium to high, ~68°) where the western domain hosts a highly localized rift with laterally persistent border fault system (Owens Valley), and the eastern domain hosts smaller paired staggered (en-echelon) rift basins (e.g., Panamint and Saline Valleys). Fault traces are from the U.S. Geological Survey and California Geological Survey, Quaternary fault and fold database (2022). Basement terranes, terrane boundaries, and shear zones are from Bateman (1968), Greene and Schweickert (1995), Dunne and Walker (2004), and Long (2012). Geodetic plate velocity vectors (black arrows) are from Bennett et al. (2003). White arrows represent the regional divergence direction taken from the largest magnitude geodetic plate motion vector at the center of the Panamint-Saline basin(Fig. 11a). HMF: Hunter Mountain Fault, PTC SZ: Proto-Kern Canyon Shear Zone, SC SZ: Sierra Crest Shear Zone, NDV, Northern Death Valley, ESTS: East Sierran Thrust System. (c) Index map with the star indicating the location of Southern Walker Lane.

orthogonally opening NW-trending rift basin along the East African Rift System (Figs. 10a&b), and the Walker Lane, an obliquely-opening NNW-trending rift zone in the Eastern California (Figs. 11a&b).

The Rukwa Rift follows the NW-trending Precambrian terranes of the Ubendian Belt and the border faults follow the terrane boundary shear zones and their surrounding metamorphic fabrics (Figs 10a,b; Daly et al., 1989; Wheeler and Karson, 1994; Lemna et al., 2019; Heilman et al., 2019; Kolawole et al., 2021a, 2021b). The development of the border faults along these shear zones suggests these shear zones represent inherited basement weak zones that localized the border faults and controlled their geometries. The present divergence direction presents a low to medium obliquity rift zone (~36°; Fig. 10a inset). More importantly, the Rukwa Rift largely developed in the Ubende Terrane, and particularly its eastern half where the border fault displacement is greatest (Fig. 10b; Morley et al., 1992). Although the Rukwa Rift is a multiphase rift with moderate rotations in extension axes over the rift phases (Delvaux et al., 2012), the rift basin generally retains a prominent rectilinearity and lateral persistence and strong coalescence of its

border faults (Fig. 10a). With the repeated failure and reactivation of the rift, the geometry of the rift faults appears to have remained the same (Kilembe and Rosendahl, 1992; Kolawole et al., 2021b), which without a detailed view of border fault vs intra-rift fault structure, could be interpreted to indicate that the host basement terranes and their shear zones are very weak. However, the intra-rift faults which have been shown to cluster along a deeply rooted intra-basement shear zone (Chisi Shear Zone, Kolawole et al., 2021a, 2021b) appear to be significantly discontinuous along-strike (Fig. 10a-b). The low obliquity extension suggests a comparison with model results in row R4 (Fig. 10a), from which we note that models R4C2 and R4C3 are most representative of the current structure of the rift zone. These model results present laterally persistent border faults and discontinuous intra-rift faults. Thus, based on the comparison of the border and intra-rift fault patterns in nature vs model results, we infer that the basement inheritance of the Rukwa Rift is within a moderately strong weak zone. Moreover, considering that the rift basin is magma-poor, an alternative explanation could be that the inherited basement weak zones are inherently mechanically weak, but that the relatively cooler lithospheric thermal regimes of the basin (Jones, 2020; Kolawole and Evenick, 2023) imposed a 'strong' crustal rheology that promoted segmentation and inhibited pronounced lateral persistence of the faults (Fagereng, 2013).

In the Walker Lane, eastern California, the present divergence direction presents a medium to high obliquity rift zone (~68°; Fig. 11a inset). The rift zone hosts tectonic domains with contrasting rifting styles (Figs. 11a,b; Wesnousky, 2005; Wesnousky and Jones, 1994). The western domain hosts the Owens Valley, which is characterized by a prominent rectilinear laterally persistent rift basin with a highly localized border fault (the Sierran Range Front Fault), and the central and eastern domains host a system of laterally discontinuous (staggered), but paired, rift basins (e.g., Panamint and Saline valleys in Fig. 11a-b; Wesnousky, 2005). The rift zone is volcanically active with magmatic centers spread across the basins (Fig. 11b). The Owens Valley developed within the Eastern Sierra Thrust Belt with a general trend that is parallel/sub-parallel to the NNW-SSE trend of the terranes (Fig. 11b). Furthermore, the Owens Valley border fault, the Sierran Range Front Fault, is co-located with the boundary between the Sierra Nevada igneous terrane and the Eastern Sierra Thrust Belt (Fig. 11b), suggesting that the fault exploited the terrane boundary. In contrast, in the central domain of the Walker Lane, the staggered NNW-trending Panamint-Saline basin system developed within the NE/NNE-trending Central Nevada Thrust Belt, which is characterized by a predominantly NE-trending structural fabric (Long, 2012). Although both the Owens Valley and the Panamint-Saline rift zone have the same structural trend and are developing within the same regional NW-SE divergence direction (Fig. 11a), their contrasting structural styles raise questions on the possible roles of distinct crustal structure and associated mechanical weaknesses beneath the rift zones. Our model results show that oblique rifts that lack laterally persistent along-strike structures or prominent fault localization characteristic of en-echelon segmented basin systems likely developed in relatively strong weak zone (e.g., Fig. 9 R1C1 - R1C4). Although this causal interpretation is plausible in the context of our model results, the segmentation of the Panamint-Saline basin system into short basins may also be attributed to their propagation across orthogonally-oriented basement fabrics of the Central Nevada Thrust Belt (Fig. 11b). In contrast to the Rukwa Rift, the Walker Lane is magma-rich, implying a relatively hotter thermal regime that should weaken the crust and promote lateral fault continuity (e.g., Fagereng, 2013); thus, suggesting that the rift structure in the central domain of the Walker Lane is likely influenced by oblique extension without the inheritance of a "weak" pre-existing weak zone (R1C2 and R1C3). In contrast, the western domain of the Walker Lane most accurately represents oblique extension that is modulated by a pre-existing weak zone, (R1C4). Overall, the reported observations from these natural active continental rifts in East Africa (Rukwa Rift; Fig. 10) and eastern California (Walker Lane; Fig. 11) provide insights into the potential controls of the strength of inherited weak zones on rift geometry and faulting patterns in both high- and low-obliquity extensional settings.

5. Conclusions

We used a 3D geodynamic model to investigate strain localization along early-stage continental rift systems that develop within inherited basement weak zones (e.g., large orogenic terranes) in low-, moderate-, and high-obliquity extensional settings. We summarize our findings as follows:

1. Depending on the strength of the inherited weak zone, rift obliquity can lead to different strain localization patterns, where low obliquity results in the development of border faults, and high obliquity generally leads to the formation of en-echelon structures.
2. The relative strength of a pre-existing weak zone plays a significant role in the large-scale patterns of strain localization, such that a pre-existing weak zone of relative lower strength leads to the development of rifts with rectilinear laterally persistent strain localization, whereas a stronger weak zone results in a staggered en-echelon structure with relatively shorter faults.
3. The strain localization patterns can be long-lived during rift evolution, persisting into the more mature rift stages where strain migrates into the center of the rift valley. Furthermore, we find that rift obliquity and weak zone strength may modulate rift fault length, throw, and azimuth.
4. *An assessment of the structure and geometry of well-studied natural rifts* that develop within orogenic basement terranes *show similarity of strain localization patterns to those in our model results, with the models providing* new and compelling insights into the *possible roles of the inherited basement strength on the* evolution of *these* rifts.

CRediT authorship contribution statement

Liang Xue: Writing – original draft, Methodology, Conceptualization. **Robert Moucha:** Writing – review & editing, Software, Methodology. **Folarin Kolawole:** Writing – original draft, Validation, Methodology. **James D. Muirhead:** Writing – review & editing, Validation, Methodology. **Christopher A. Scholz:** Writing – review & editing, Validation, Supervision.

Declaration of competing interest

None.

Data availability

No data was used for the research described in the article.

Acknowledgment

This research was supported by NSF-EAR-2116017 to CAS and RM, grants from Chevron and Petrobras grants to CAS, and Syracuse University. We thank Frank Zwaan,the anonymous reviewer, and editor Claire A Currie for their comments and suggestions. The ASPECT code is available from Computational Infrastructure for Geodynamics (aspect.geodynamics.org/). The fault statistical analysis tool fatbox is available from (https://github.com/thilowrona/fatbox).

References

Agostini, A., Corti, G., Zeoli, A., Mulugeta, G., 2009. Evolution, pattern, and partitioning of deformation during oblique continental rifting: inferences from lithospheric-scale centrifuge models: centrifuge models of oblique rifting. Geochem. Geophys. Geosyst. 10 (11) https://doi.org/10.1029/2009GC002676.

Agostini, S., Doglioni, C., Innocenti, F., Manetti, P., Tonarini, S., 2010. On the geodynamics of the Aegean rift. Tectonophysics 488 (1–4), 7–21. https://doi.org/10.1016/j.tecto.2009.07.025.

Agostini, A., Bonini, M., Corti, G., Sani, F., Manetti, P., 2011. Distribution of quaternary deformation in the Central Main Ethiopian Rift, East Africa: deformation in the Main Ethiopian Rift. Tectonics 30 (4). https://doi.org/10.1029/2010TC002833.

Allken, V., Huismans, R.S., Thieulot, C., 2011. Three-dimensional numerical modeling of upper crustal extensional systems. J. Geophys. Res. Solid Earth 116 (B10).

Ammann, N., Liao, J., Gerya, T., Ball, P., 2018. Oblique continental rifting and long transform fault formation based on 3D thermomechanical numerical modeling. Tectonophysics 746, 106–120. https://doi.org/10.1016/j.tecto.2017.08.015.

Anderson, E.M., 1905. The dynamics of faulting. Trans. Edinb. Geol. Soc. 8 (3), 387–402.

Andrés-Martínez, M., Pérez-Gussinyé, M., Armitage, J., Morgan, J.P., 2019. Thermomechanical implications of sediment transport for the architecture and evolution of continental rifts and margins. Tectonics 38 (2), 641–665. https://doi.org/10.1029/2018TC005346.

Argus, D.F., Gordon, R.G., DeMets, C., 2011. Geologically current motion of 56 plates relative to the no-net-rotation reference frame: NNR-MORVEL56. Geochem. Geophys. Geosyst. 12 (11) https://doi.org/10.1029/2011GC003751.

Autin, J., Bellahsen, N., Leroy, S., Husson, L., Beslier, M.O., d'Acremont, E., 2013. The role of structural inheritance in oblique rifting: insights from analogue models and application to the Gulf of Aden. Tectonophysics 607, 51–64. https://doi.org/10.1016/j.tecto.2013.05.041.

Basile, C., Brun, J.P., 1999. Transtensional faulting patterns ranging from pull-apart basins to transform continental margins: an experimental investigation. J. Struct. Geol. 21 (1), 23–37. https://doi.org/10.1016/S0191-8141(98)00094-7.

Bateman, P.C., 1968. Geologic structure and history of the Sierra Nevada. UMR J. 1 (1), 121–132. VH McNutt Colloq. Ser.

Bellahsen, N., Leroy, S., Autin, J., Razin, P., d'Acremont, E., Sloan, H., Pik, R., Ahmed, A., Khanbari, K., 2013. Pre-existing oblique transfer zones and transfer/transform relationships in continental margins: new insights from the southeastern Gulf of Aden, Socotra Island, Yemen. Tectonophysics 607, 32–50. https://doi.org/10.1016/j.tecto.2013.07.036.

Bennett, R.A., Wernicke, B.P., Niemi, N.A., Friedrich, A.M., Davis, J.L., 2003. Contemporary strain rates in the northern basin and range province from GPS data. Tectonics 22 (2).

Bonini, M., Souriot, T., Boccaletti, M., Brun, J.P., 1997. Successive orthogonal and oblique extension episodes in a rift zone: laboratory experiments with application to the Ethiopian Rift. Tectonics 16 (2), 347–362. https://doi.org/10.1029/96TC03935.

Bonini, M., Cerca, M., Moratti, G., López-Martínez, M., Corti, G., Gracia-Marroquín, D., 2019. Strain partitioning in highly oblique rift settings: inferences from the southwestern margin of the Gulf of California (Baja California Sur, México). Tectonics 38 (12), 4426–4453. https://doi.org/10.1029/2019TC005566.

Bonini, L., Fracassi, U., Bertone, N., Maesano, F.E., Valensise, G., Basili, R., 2023. How do inherited dip-slip faults affect the development of new extensional faults? Insights from wet clay analog models. J. Struct. Geol. 169, 104836.

Brune, S., 2014. Evolution of stress and fault patterns in oblique rift systems: 3-D numerical lithospheric-scale experiments from rift to breakup. Geochem. Geophys. Geosyst. 15 (8), 3392–3415. https://doi.org/10.1002/2014GC005446.

Brune, S., Popov, A.A., Sobolev, S.V., 2012. Modeling suggests that oblique extension facilitates rifting and continental break-UP: oblique extension facilitates rifting and break-up. J. Geophys. Res. Solid Earth 117 (B8), n/a. https://doi.org/10.1029/2011JB008860.

Brune, S., Corti, G., Ranalli, G., 2017a. Controls of inherited lithospheric heterogeneity on rift linkage: numerical and analog models of interaction between the Kenyan and Ethiopian rifts across the Turkana depression: rift linkage modeling, Turkana Region. Tectonics 36 (9), 1767–1786. https://doi.org/10.1002/2017TC004739.

Brune, S., Williams, S.E., Müller, R.D., 2017b. Potential links between continental rifting, CO2 degassing and climate change through time. Nat. Geosci. 10 (12), 941–946. https://doi.org/10.1038/s41561-017-0003-6.

Brune, S., Williams, S.E., Müller, R.D., 2018. Oblique rifting: the rule, not the exception. Solid Earth 9 (5), 1187–1206. https://doi.org/10.5194/se-9-1187-2018.

Chapman, D.S., 1986. Thermal gradients in the continental crust. Geol. Soc. Lond. Spec. Publ. 24 (1), 63–70. https://doi.org/10.1144/GSL.SP.1986.024.01.07.

Chorowicz, J., Sorlien, C., 1992. Oblique extensional tectonics in the Malawi Rift, Africa. Geol. Soc. Am. Bull. 104 (8), 1015–1023. https://doi.org/10.1130/0016-7606(1992)104<1015:OETITM>2.3.CO;2.

Clifton, A.E., Schlische, R.W., Withjack, M.O., Ackermann, R.V., 2000. Influence of rift obliquity on fault-population systematics: results of experimental clay models. J. Struct. Geol. 22 (10), 1491–1509. https://doi.org/10.1016/S0191-8141(00)00043-2.

Corti, G., 2008. Control of rift obliquity on the evolution and segmentation of the main Ethiopian rift. Nat. Geosci. 1 (4), 258–262.

Corti, G., Van Wijk, J., Bonini, M., Sokoutis, D., Cloetingh, S., Innocenti, F., Manetti, P., 2003. Transition from continental break-up to punctiform seafloor spreading: how fast, symmetric and magmatic: from break-up to punctiform spreading. Geophys. Res. Lett. 30 (12) https://doi.org/10.1029/2003GL017374.

Corti, G., Calignano, E., Petit, C., Sani, F., 2011. Controls of lithospheric structure and plate kinematics on rift architecture and evolution: an experimental modeling of the Baikal rift: experimental modeling of the Baikal rift. Tectonics 30 (3), n/a–n/a. https://doi.org/10.1029/2011TC002871.

Corti, G., Philippon, M., Sani, F., Keir, D., Kidane, T., 2013. Re-orientation of the extension direction and pure extensional faulting at oblique rift margins: comparison between the Main Ethiopian Rift and laboratory experiments. Terra Nova 25 (5), 396–404. https://doi.org/10.1111/ter.12049.

Corti, G., Sani, F., Agostini, S., Philippon, M., Sokoutis, D., Willingshofer, E., 2018. Off-axis volcano-tectonic activity during continental rifting: insights from the transversal Goba-Bonga lineament, Main Ethiopian Rift (East Africa). Tectonophysics 728–729, 75–91. https://doi.org/10.1016/j.tecto.2018.02.011.

Corti, G., Cioni, R., Franceschini, Z., Sani, F., Scaillet, S., Molin, P., Isola, I., Mazzarini, F., Brune, S., Keir, D., Erbello, A., Muluneh, A., Illsley-Kemp, F., Glerum, A., 2019. Aborted propagation of the Ethiopian rift caused by linkage with the Kenyan rift. Nat. Commun. 10 (1), 1309. https://doi.org/10.1038/s41467-019-09335-2.

Corti, G., Maestrelli, D., Sani, F., 2022. Large-to local-scale control of pre-existing structures on continental rifting: examples from the Main Ethiopian Rift, East Africa. Front. Earth Sci. 10, 808503.

Courtillot, V., 1982. Propagating rifts and continental breakup. Tectonics 1 (3), 239–250. https://doi.org/10.1029/TC001i003p00239.

Cruz-Hernández, F., Castro-Escamilla, R.R., Mendoza-Camberos, J.A., Pérez-Vertti, A., 2023. Seismicity and state of stress in the north-central region of the Gulf of California, Mexico. Tectonophysics 863, 230020.

Daly, M.C., 1988. Crustal shear zones in Central Africa: a kinematic approach to proterozoic tectonics. Episodes 11 (1), 5–11.

Daly, M.C., Chorowicz, J., Fairhead, J.D., 1989. Rift basin evolution in Africa: the influence of reactivated steep basement shear zones. Geol. Soc. Lond. Spec. Publ. 44 (1), 309–334.

Dauteuil, O., Brun, J.P., 1993. Oblique rifting in a slow-spreading ridge. Nature 361 (6408), 145–148. https://doi.org/10.1038/361145a0.

Dauteuil, O., Bourgeois, O., Mauduit, T., 2002. Lithosphere strength controls oceanic transform zone structure: Insights from analogue models. Geophys. J. Int. 150 (3), 706–714. https://doi.org/10.1046/j.1365-246X.2002.01736.x.

Davis, R.O., Selvadurai, A.P.S., 2002. Plasticity and Geomechanics, 1st ed. Cambridge University Press. https://doi.org/10.1017/CBO9780511614958.

Delvaux, D., Barth, A., 2010. African stress pattern from formal inversion of focal mechanism data. Tectonophysics 482 (1–4), 105–128.

Delvaux, D., Kervyn, F., Macheyeki, A.S., Temu, E.B., 2012. Geodynamic significance of the TRM segment in the East African Rift (W-Tanzania): active tectonics and paleostress in the ufipa plateau and Rukwa basin. J. Struct. Geol. 37, 161–180.

Díaz-Azpiroz, M., Brune, S., Leever, K.A., Fernández, C., Czeck, D.M., 2016. Tectonics of oblique plate boundary systems. Tectonophysics 693, 165–170. https://doi.org/10.1016/j.tecto.2016.07.028.

Duclaux, G., Huismans, R.S., May, D.A., 2020. Rotation, narrowing, and preferential reactivation of brittle structures during oblique rifting. Earth Planet. Sci. Lett. 531, 115952 https://doi.org/10.1016/j.epsl.2019.115952.

Dunne, G.C., Walker, J.D., 2004. Structure and evolution of the East Sierran thrust system, East Central California. Tectonics 23 (4).

Dyksterhuis, S., Rey, P., Müller, R.D., Moresi, L., 2007. Effects of initial weakness on rift architecture. Geol. Soc. Lond. Spec. Publ. 282 (1), 443–455.

Ebinger, C., van Wijk, J., 2014. Roadmap to continental rupture: is obliquity the route to success? Geology 42 (3), 271–272.

Fagereng, Å., 2013. Fault segmentation, deep rift earthquakes and crustal rheology: insights from the 2009 Karonga sequence and seismicity in the Rukwa–Malawi rift zone. Tectonophysics 601, 216–225.

Ferrari, L., 2013. Late oligocene to middle miocene rifting and syn-extensional magmatism in the southwestern Sierra Madre Occidental, Mexico: the beginning of the Gulf of California rift. Geosphere 9 (5), 1161. https://doi.org/10.1130/GES00925.1.

Fritz, H., Abdelsalam, M., Ali, K.A., Bingen, B., Collins, A.S., Fowler, A.R., et al., 2013. Orogen styles in the East African Orogen: a review of the Neoproterozoic to Cambrian tectonic evolution. J. Afr. Earth Sci. 86, 65–106.

Fuchs, L., Becker, T.W., 2021. Deformation memory in the lithosphere: a comparison of damage-dependent weakening and grain-size sensitive rheologies. J. Geophys. Res. Solid Earth 126 (1). https://doi.org/10.1029/2020JB020335.

Gassmöller, R., Lokavarapu, H., Heien, E., Puckett, E.G., Bangerth, W., 2018. Flexible and scalable particle-in-cell methods with adaptive mesh refinement for geodynamic computations. Geochem. Geophys. Geosyst. 19 (9), 3596–3604. https://doi.org/10.1029/2018GC007508.

Glerum, A., Thieulot, C., Fraters, M., Blom, C., Spakman, W., 2018. Nonlinear viscoplasticity in ASPECT: benchmarking and applications to subduction. Solid Earth 9 (2), 267–294. https://doi.org/10.5194/se-9-267-2018.

Glerum, A., Brune, S., Stamps, D.S., Strecker, M.R., 2020. Victoria continental microplate dynamics controlled by the lithospheric strength distribution of the East African Rift. Nat. Commun. 11 (1), 2881. https://doi.org/10.1038/s41467-020-16176-x.

Gouiza, M., Naliboff, J., 2021. Rheological inheritance controls the formation of segmented rifted margins in cratonic lithosphere. Nat. Commun. 12 (1), 4653. https://doi.org/10.1038/s41467-021-24945-5.

Greene, D.C., Schweickert, R.A., 1995. The Gem Lake shear zone: cretaceous dextral transpression in the northern Ritter Range pendant, eastern Sierra Nevada, California. Tectonics 14 (4), 945–961.

Grijalva, A., Nyblade, A.A., Homman, K., Accardo, N.J., Gaherty, J.B., Ebinger, C.J., Tepp, G., 2018. Seismic evidence for plume-and craton-influenced upper mantle structure beneath the northern Malawi Rift and the Rungwe Volcanic Province, East Africa. Geochem. Geophys. Geosyst. 19 (10), 3980–3994.

Grimmer, J.C., Ritter, J.R.R., Eisbacher, G.H., Fielitz, W., 2017. The late variscan control on the location and asymmetry of the Upper Rhine Graben. Int. J. Earth Sci. 106, 827–853.

Gueydan, F., Morency, C., Brun, J.P., 2008. Continental rifting as a function of lithosphere mantle strength. Tectonophysics 460 (1–4), 83–93.

Heilman, E., Kolawole, F., Atekwana, E.A., Mayle, M., 2019. Controls of basement fabric on the linkage of rift segments. Tectonics 38 (4), 1337–1366.

Heine, C., Brune, S., 2014. Oblique rifting of the equatorial Atlantic: why there is no Saharan Atlantic Ocean. Geology 42 (3), 211–214. https://doi.org/10.1130/G35082.1.
Heister, T., Dannberg, J., Gassmöller, R., Bangerth, W., 2017. High accuracy mantle convection simulation through modern numerical methods – II: realistic models and problems. Geophys. J. Int. 210 (2), 833–851. https://doi.org/10.1093/gji/ggx195.
Henza, A.A., Withjack, M.O., Schlische, R.W., 2011. How do the properties of a pre-existing normal-fault population influence fault development during a subsequent phase of extension? J. Struct. Geol. 33 (9), 1312–1324.
Jones, D.J.R., 2020. A Summary of the East Africa Rift Temperature and Heat Flow Model (EARTH).
Jourdon, A., Le Pourhiet, L., Mouthereau, F., May, D., 2020. Modes of propagation of continental breakup and associated oblique rift structures. J. Geophys. Res. Solid Earth 125 (9). https://doi.org/10.1029/2020JB019906.
Katumwehe, A.B., Abdelsalam, M.G., Atekwana, E.A., 2015. The role of pre-existing precambrian structures in rift evolution: the Albertine and Rhino grabens, Uganda. Tectonophysics 646, 117–129.
Kilembe, E.A., Rosendahl, B.R., 1992. Structure and stratigraphy of the Rukwa Rift. In: Ebinger, C.J., Gupta, H.K., Nyambok, L.O. (Eds.), Tectonophysics, 209. Seismology and Related Sciences in Africa, Nairobi, Kenya, pp. 143–158.
Kinabo, B.D., Atekwana, E.A., Hogan, J.P., Modisi, M.P., Wheaton, D.D., Kampunzu, A. B., 2007. Early structural development of the Okavango rift zone, NW Botswana. J. Afr. Earth Sci. 48 (2–3), 125–136.
Kolawole, F., Evenick, J.C., 2023. Global distribution of geothermal gradients in sedimentary basins. Geosci. Front. 14 (6), 101685.
Kolawole, F., Atekwana, E.A., Laó-Dávila, D.A., Abdelsalam, M.G., Chindandali, P.R., Salima, J., Kalindekafe, L., 2018. Active deformation of Malawi Rift's North Basin Hinge Zone modulated by reactivation of preexisting precambrian shear zone fabric. Tectonics 37 (3), 683–704. https://doi.org/10.1002/2017TC004628.
Kolawole, F., Firkins, M.C., Al Wahaibi, T.S., Atekwana, E.A., Soreghan, M.J., 2021a. Rift interaction zones and the stages of rift linkage in active segmented continental rift systems. Basin Res. 33, 2984–3020.
Kolawole, F., Phillips, T.B., Atekwana, E.A., Jackson, C.A.L., 2021b. Structural inheritance controls strain distribution during early continental rifting, Rukwa rift. Front. Earth Sci. 670.
Kolawole, F., Vick, T., Atekwana, E.A., Laó-Dávila, D.A., Costa, A.G., Carpenter, B.M., 2022. Strain localization and migration during the pulsed lateral propagation of the Shire Rift Zone, East Africa. Tectonophysics 839, 229499.
Koptev, A., Calais, E., Burov, E., Leroy, S., Gerya, T., 2015. Dual continental rift systems generated by plume–lithosphere interaction. Nat. Geosci. 8 (5), 388–392. https://doi.org/10.1038/ngeo2401.
Kreemer, C., Holt, W.E., Haines, A.J., 2003. An integrated global model of present-day plate motions and plate boundary deformation. Geophys. J. Int. 154 (1), 8–34. https://doi.org/10.1046/j.1365-246X.2003.01917.x.
Kronbichler, M., Heister, T., Bangerth, W., 2012. High accuracy mantle convection simulation through modern numerical methods: high accuracy mantle convection simulation. Geophys. J. Int. 191 (1), 12–29. https://doi.org/10.1111/j.1365-246X.2012.05609.x.
Laó-Dávila, D.A., Al-Salmi, H.S., Abdelsalam, M.G., Atekwana, E.A., 2015. Hierarchical segmentation of the Malawi Rift: the influence of inherited lithospheric heterogeneity and kinematics in the evolution of continental rifts. Tectonics 34 (12), 2399–2417. https://doi.org/10.1002/2015TC003953.
Lavayssière, A., Drooff, C., Ebinger, C.J., Gallacher, R., Illsley-Kemp, F., Oliva, S.J., Keir, D., 2019. Depth extent and kinematics of faulting in the Southern Tanganyika Rift, Africa. Tectonics 38, 842–862.
Le Pourhiet, L., May, D.A., Huille, L., Watremez, L., Leroy, S., 2017. A genetic link between transform and hyper-extended margins. Earth Planet. Sci. Lett. 465, 184–192. https://doi.org/10.1016/j.epsl.2017.02.043.
Lemna, O.S., Stephenson, R., Cornwell, D.G., 2019. The role of pre-existing precambrian structures in the development of Rukwa Rift Basin, Southwest Tanzania. J. Afr. Earth Sci. 150, 607–625.
Lenoir, J.L., Liégeois, J.-P., Theunissen, K., Klerkx, J., 1994. The palaeoproterozoic ubendian shear belt in Tanzania: geochronology and structure. J. Afr. Earth Sci. 19 (3), 169–184.
Liu, Z., Pérez-Gussinyé, M., Rüpke, L., Muldashev, I.A., Minshull, T.A., Bayrakci, G., 2022. Lateral coexistence of ductile and brittle deformation shapes magma-poor distal margins: an example from the West Iberia-Newfoundland margins. Earth Planet. Sci. Lett. 578, 117288 https://doi.org/10.1016/j.epsl.2021.117288.
Long, S.P., 2012. Magnitudes and spatial patterns of erosional exhumation in the Sevier hinterland, eastern Nevada and western Utah, USA: insights from a paleogene paleogeologic map. Geosphere 8 (4), 881–901.
Maestrelli, D., Brune, S., Corti, G., Keir, D., Muluneh, A.A., Sani, F., 2022. Analog and numerical modeling of rift-rift-rift triple junctions. Tectonics 41 (10). https://doi.org/10.1029/2022TC007491.
McClay, K.R., White, M.J., 1995. Analogue modelling of orthogonal and oblique rifting. Mar. Pet. Geol. 12 (2), 137–151. https://doi.org/10.1016/0264-8172(95)92835-K.
Michon, L., Merle, O., 2000. Crustal structures of the Rhinegraben and the Massif Central grabens: an experimental approach. Tectonics 19 (5), 896–904. https://doi.org/10.1029/2000TC900015.
Molnar, N.E., Cruden, A.R., Betts, P.G., 2018. Unzipping continents and the birth of microcontinents. Geology 46 (5), 451–454.
Molnar, N.E., Cruden, A.R., Betts, P.G., 2019. Interactions between propagating rifts and linear weaknesses in the lower crust. Geosphere 15 (5), 1617–1640. https://doi.org/10.1130/GES02119.1.
Molnar, N., Cruden, A., Betts, P., 2020. The role of inherited crustal and lithospheric architecture during the evolution of the Red Sea: insights from three dimensional analogue experiments. Earth Planet. Sci. Lett. 544, 116377.
Morgan, P., Seager, W.R., Golombek, M.P., 1986. Cenozoic thermal, mechanical and tectonic evolution of the Rio Grande Rift. J. Geophys. Res. 91 (B6), 6263. https://doi.org/10.1029/JB091iB06p06263.
Morley, C.K., Cunningham, S.M., Harper, R.M., Wescott, W.A., 1992. Geology and geophysics of the Rukwa Rift, East Africa. Tectonics 11 (1), 69–81.
Morley, C.K., Wescott, W.A., Harper, R.M., Cunningham, S.M., 1999. Geology and geophysics of the Rukwa Rift. Geoscience of rift systems-evolution of East Africa. AAPG Stud. Geol. 44, 91–110.
Morley, C.K., Haranya, C., Phoosongsee, W., Pongwapee, S., Kornsawan, A., Wonganan, N., 2004. Activation of rift oblique and rift parallel pre-existing fabrics during extension and their effect on deformation style: examples from the rifts of Thailand. J. Struct. Geol. 26 (10), 1803–1829.
Muirhead, J.D., Kattenhorn, S.A., 2018. Activation of preexisting transverse structures in an evolving magmatic rift in East Africa. J. Struct. Geol. 106, 1–18.
Muirhead, J.D., Wright, L.J.M., Scholz, C.A., 2019. Rift evolution in regions of low magma input in East Africa. Earth Planet. Sci. Lett. 506, 332–346. https://doi.org/10.1016/j.epsl.2018.11.004.
Müller, R.D., Seton, M., Zahirovic, S., Williams, S.E., Matthews, K.J., Wright, N.M., Shephard, G.E., Maloney, K.T., Barnett-Moore, N., Hosseinpour, M., Bower, D.J., Cannon, J., 2016. Ocean basin evolution and global-scale plate reorganization events since pangea breakup. Annu. Rev. Earth Planet. Sci. 44 (1), 107–138. https://doi.org/10.1146/annurev-earth-060115-012211.
Naliboff, J.B., Glerum, A., Brune, S., Péron-Pinvidic, G., Wrona, T., 2020. Development of 3-D rift heterogeneity through fault network evolution. Geophys. Res. Lett. 47 (13) https://doi.org/10.1029/2019GL086611.
Neuharth, D., Brune, S., Glerum, A., Heine, C., Welford, J.K., 2021. Formation of continental microplates through rift linkage: numerical modeling and its application to the flemish cap and Sao Paulo Plateau. Geochem. Geophys. Geosyst. 22 (4) https://doi.org/10.1029/2020GC009615.
Neuharth, D., Brune, S., Wrona, T., Glerum, A., Braun, J., Yuan, X., 2022. Evolution of rift systems and their fault networks in response to surface processes. Tectonics 41 (3). https://doi.org/10.1029/2021TC007166.
Nixon, C.W., McNeill, L.C., Bull, J.M., Bell, R.E., Gawthorpe, R.L., Henstock, T.J., Christodoulou, D., Ford, M., Taylor, B., Sakellariou, D., Ferentinos, G., Papatheodorou, G., Leeder, M.R., Collier, R.E., Goodliffe, A.M., Sachpazi, M., Kranis, H., 2016. Rapid spatiotemporal variations in rift structure during development of the Corinth Rift, Central Greece: rapid changes in Rift Structure, Corinth. Tectonics 35 (5), 1225–1248. https://doi.org/10.1002/2015TC004026.
Njinju, E.A., Stamps, D.S., Neumiller, K., Gallager, J., 2021. Lithospheric control of melt generation beneath the Rungwe Volcanic Province, East Africa: implications for a Plume Source. J. Geophys. Res. Solid Earth 126 (5). https://doi.org/10.1029/2020JB020728.
Olive, J.A., Malatesta, L.C., Behn, M.D., Buck, W.R., 2022. Sensitivity of rift tectonics to global variability in the efficiency of river erosion. Proc. Natl. Acad. Sci. 119 (13), e2115077119 https://doi.org/10.1073/pnas.2115077119.
Osagiede, E.E., Rosenau, M., Rotevatn, A., Gawthorpe, R., Jackson, C.A., Rudolf, M., 2021. Influence of zones of pre-existing crustal weakness on strain localization and partitioning during rifting: insights from analog modeling using high-resolution 3D digital image correlation. Tectonics 40 (10). https://doi.org/10.1029/2021TC006970.
Pasyanos, M.E., Masters, T.G., Laske, G., Ma, Z., 2014. LITHO1.0: an updated crust and lithospheric model of the Earth. J. Geophys. Res. Solid Earth 119 (3), 2153–2173. https://doi.org/10.1002/2013JB010626.
Philippon, M., Corti, G., 2016. Obliquity along plate boundaries. Tectonophysics 693, 171–182. https://doi.org/10.1016/j.tecto.2016.05.033.
Philippon, M., Willingshofer, E., Sokoutis, D., Corti, G., Sani, F., Bonini, M., Cloetingh, S., 2015. Slip re-orientation in oblique rifts. Geology 43 (2), 147–150. https://doi.org/10.1130/G36208.1.
Phillips, T.B., Fazlikhani, H., Gawthorpe, R.L., Fossen, H., Jackson, C.A.L., Bell, R.E., Faleide, J.I., Rotevatn, A., 2019. The influence of structural inheritance and multiphase extension on rift development, the Northern North Sea. Tectonics 38.
Phillips, T.B., Naliboff, J.B., McCaffrey, K.J., Pan, S., van Hunen, J., Froemchen, M., 2023. The influence of crustal strength on rift geometry and development–insights from 3D numerical modelling. Solid Earth 14 (4), 369–388.
Pichel, L.M., Huismans, R.S., Gawthorpe, R., Faleide, J.I., Theunissen, T., 2022. Coupling crustal-scale rift architecture with passive margin salt tectonics: a geodynamic modeling approach. J. Geophys. Res. Solid Earth 127 (11). https://doi.org/10.1029/2022JB025177.
Plattner, C., Malservisi, R., Dixon, T.H., LaFemina, P., Sella, G.F., Fletcher, J., Suarez-Vidal, F., 2007. New constraints on relative motion between the Pacific Plate and Baja California microplate (Mexico) from GPS measurements. Geophys. J. Int. 170 (3), 1373–1380.
Rajaonarison, T.A., Stamps, D.S., Naliboff, J., 2021. Role of lithospheric buoyancy forces in driving deformation in east africa from 3D geodynamic modeling. Geophys. Res. Lett. 48 (6) https://doi.org/10.1029/2020GL090483.
Reeve, M.T., Bell, R.E., Duffy, O.B., Jackson, C.A.L., Sansom, E., 2015. The growth of non-colinear normal fault systems; What can we learn from 3D seismic reflection data? J. Struct. Geol. 70, 141–155.
Richetti, P.C., Zwaan, F., Schreurs, G., Schmitt, R.S., Schmid, T.C., 2023. Analogue modelling of basin inversion: implications for the Araripe Basin (Brazil). Solid Earth 14 (12), 1245–1266.
Richter, M.J.E.A., Brune, S., Riedl, S., Glerum, A., Neuharth, D., Strecker, M.R., 2021. Controls on asymmetric rift dynamics: numerical modeling of strain localization and

fault evolution in the Kenya Rift. Tectonics 40 (5). https://doi.org/10.1029/2020TC006553.
Rose, I., Buffett, B., Heister, T., 2017. Stability and accuracy of free surface time integration in viscous flows. Phys. Earth Planet. Inter. 262, 90–100. https://doi.org/10.1016/j.pepi.2016.11.007.
Samsu, A., Micklethwaite, S., Williams, J.N., Fagereng, Å., Cruden, A.R., 2023. Structural inheritance in amagmatic rift basins: manifestations and mechanisms for how pre-existing structures influence rift-related faults. Earth Sci. Rev. 246, 104568. https://doi.org/10.1016/j.earscirev.2023.104568.
Sarafian, E., Evans, R.L., Abdelsalam, M.G., Atekwana, E., Elsenbeck, J., Jones, A.G., Chikambwe, E., 2018. Imaging Precambrian lithospheric structure in Zambia using electromagnetic methods. Gondwana Res. 54, 38–49.
Schmid, T.C., Brune, S., Glerum, A., Schreurs, G., 2023. Tectonic interactions during rift linkage: insights from analog and numerical experiments. Solid Earth 14 (4), 389–407.
Shaban, S.N., Kolawole, F., Scholz, C.A., 2023. the deep basin and underlying basement structure of the Tanganyika rift. Tectonics 42 (7), e2022TC007726.
Stamps, D.S., Calais, E., Saria, E., Hartnady, C., Nocquet, J.M., Ebinger, C.J., Fernandes, R.M., 2008. A kinematic model for the East African Rift. Geophys. Res. Lett. 35 (5).
Stamps, D.S., Saria, E., Kreemer, C., 2018. A geodetic strain rate model for the East African Rift system. Sci. Rep. 8 (1), 732.
Tozer, B., Sandwell, D.T., Smith, W.H., Olson, C., Beale, J.R., Wessel, P., 2019. Global bathymetry and topography at 15 arc sec: SRTM15+. Earth Space Sci. 6 (10), 1847–1864.
Van Wijk, J.W., 2005. Role of weak zone orientation in continental lithosphere extension. Geophys. Res. Lett. 32 (2), L02303 https://doi.org/10.1029/2004GL022192.
Van Wijk, J., Axen, G., Abera, R., 2017. Initiation, evolution and extinction of pull-apart basins: implications for opening of the Gulf of California. Tectonophysics 719, 37–50.
Versfelt, J., Rosendahl, B.R., 1989. Relationships between pre-rift structure and rift architecture in Lakes Tanganyika and Malawi, East Africa. Nature 337 (6205), 354–357. https://doi.org/10.1038/337354a0.
Vink, G.E., 1982. Continental rifting and the implications for plate tectonic reconstructions. J. Geophys. Res. Solid Earth 87 (B13), 10677–10688. https://doi.org/10.1029/JB087iB13p10677.
Wadge, G., Biggs, J., Lloyd, R., Kendall, J.M., 2016. Historical volcanism and the state of stress in the East African Rift System. Front. Earth Sci. 4, 86.
Wang, L., Maestrelli, D., Corti, G., Zou, Y., Shen, C., 2021. Normal fault reactivation during multiphase extension: analogue models and application to the Turkana depression, East Africa. Tectonophysics 811, 228870.
Wesnousky, S.G., 2005. The San Andreas and Walker Lane fault systems, western North America: transpression, transtension, cumulative slip and the structural evolution of a major transform plate boundary. J. Struct. Geol. 27 (8), 1505–1512.
Wesnousky, S.G., Jones, C.H., 1994. Oblique slip, slip partitioning, spatial and temporal changes in the regional stress field, and the relative strength of active faults in the Basin and Range, western United States. Geology 22 (11), 1031–1034.
Wheeler, W., Karson, J., 1989. Structure and kinematics of the livingstone mountains border fault zone, Nyasa (Malawi) Rift, southwestern Tanzania. J. Afr. Earth Sci. 8, 393–413.
Wheeler, W.H., Karson, J.A., 1994. Extension and subsidence adjacent to a "weak" continental transform: an example from the Rukwa Rift, East Africa. Geol 22 (7), 625–628.
Withjack, M.O., Schlische, R.W., Olsen, P.E., 2002. Rift-basin structure and its influence on sedimentary systems. Soc. Sediment. Geol. Spec. Publ. 73 (2002), 57–81.
Wolf, L., Huismans, R.S., Rouby, D., Gawthorpe, R.L., Wolf, S.G., 2022. Links between faulting, topography, and sediment production during continental rifting: insights from coupled surface process, thermomechanical modeling. J. Geophys. Res. Solid Earth 127 (3). https://doi.org/10.1029/2021JB023490.
Wrona, T., Brune, S., Gayrin, P., Hake, T., 2022. Fatbox—Fault Analysis Toolbox (0.1-Alpha), [Computer software]. GFZ Data Services. https://doi.org/10.5880/GFZ.2.5.2022.002.
Zou, Y., Maestrelli, D., Corti, G., Del Ventisette, C., Wang, L., Shen, C., 2024. Influence of inherited brittle fabrics on continental rifting: insights from centrifuge experimental modeling and application to the East African Rift system. Tectonics 43 (1), e2023TC007947.
Zwaan, F., Schreurs, G., 2017. How oblique extension and structural inheritance influence rift segment interaction: insights from 4D analog models. Interpretation 5 (1), SD119–SD138. https://doi.org/10.1190/INT-2016-0063.1.
Zwaan, F., Schreurs, G., 2020. Rift segment interaction in orthogonal and rotational extension experiments: implications for the large-scale development of rift systems. J. Struct. Geol. 140, 104119 https://doi.org/10.1016/j.jsg.2020.104119.
Zwaan, F., Schreurs, G., 2023. The link between Somalian Plate rotation and the East African Rift system: an analogue modelling study. Solid Earth 14 (8), 823–845.
Zwaan, F., Schreurs, G., Naliboff, J., Buiter, S.J.H., 2016. Insights into the effects of oblique extension on continental rift interaction from 3D analogue and numerical models. Tectonophysics 693, 239–260. https://doi.org/10.1016/j.tecto.2016.02.036.
Zwaan, F., Schreurs, G., Adam, J., 2018. Effects of sedimentation on rift segment evolution and rift interaction in orthogonal and oblique extensional settings: insights from analogue models analysed with 4D X-ray computed tomography and digital volume correlation techniques. Glob. Planet. Chang. 171, 110–133. https://doi.org/10.1016/j.gloplacha.2017.11.002.
Zwaan, F., Schreurs, G., Rosenau, M., 2020. Rift propagation in rotational versus orthogonal extension: Insights from 4D analogue models. J. Struct. Geol. 135, 103946.
Zwaan, F., Chenin, P., Erratt, D., Manatschal, G., Schreurs, G., 2021. Complex rift patterns, a result of interacting crustal and mantle weaknesses, or multiphase rifting? Insights from analogue models. Solid Earth Discuss. 2021, 1–38.
Zwaan, F., Chenin, P., Erratt, D., Manatschal, G., Schreurs, G., 2022. Competition between 3D structural inheritance and kinematics during rifting: insights from analogue models. Basin Res. 34 (2), 824–854. https://doi.org/10.1111/bre.12642.
Zwaan, F., Erratt, D., Manatschal, G., Chenin, P., Schreurs, G., 2024. On the delayed expression of mantle inheritance–controlled strain localization during rifting. Geology 2024. https://doi.org/10.1130/G52309.1.